ATOMISTIC SIMULATION OF CHARGE EFFECTS: FROM TUNABLE THIN FILM GROWTH TO ISOLATION OF SURFACE STATES WITH SPIN-ORBIT COUPLING

by

Wenmei Ming

A dissertation submitted to the faculty of
The University of Utah
in partial fulfillment of the requirements for the degree of

Doctor of Philosophy

Department of Materials Science and Engineering

The University of Utah

May 2015

The University of Utah Graduate School

STATEMENT OF DISSERTATION APPROVAL

The dissertation of **Wenmei Ming**

has been approved by the following supervisory committee members:

Feng Liu	, Chair	**01/08/2015** Date Approved
Ashutosh Tiwari	, Member	**01/06/2015** Date Approved
Ling Zang	, Member	**01/06/2015** Date Approved
Zhigang Zak Fang	, Member	**01/06/2015** Date Approved
Yong-Shi Wu	, Member	**01/06/2015** Date Approved

and by **Feng Liu** , Chair/Dean of

the Department/College/School of **Materials Science and Engineering**

and by David B. Kieda, Dean of The Graduate School.

ABSTRACT

This dissertation revitalizes the importance of surface charge effects in semiconductor nanostructures, in particular in the context of thin film growth and exotic electronic structures under delicate spin-orbit coupling. A combination of simulation techniques, including density functional theory calculation, kinetic Monte Carlo method, nonequilibrium Green's function method, and tight binding method, were employed to reveal the underlying physical mechanisms of four topics: (1) Effects of Li doping on H-diffusion in MgH_2 for hydrogen storage. It addresses both the effect of Fermi level tuning by charged dopant and the effect of dopant-defect interaction, and the latter was largely neglected in previous works; (2) Tuning nucleation density of the metal island with charge doping of the graphene substrate. It is the first time that the surface charge doping effect is proposed and studied as an effective approach to tune the kinetics of island nucleation at the early stage of thin film growth; (3) Complete isolation of Rashba surface states on the saturated semiconductor surface. It shows that the naturally saturated semiconductor surface of InSe(0001) with Au single layer film provides a mechanism for the formation of Rashba states with large spin splitting; it opens up an innovative route to obtaining ideal Rashba states without the overwhelming bulk spin-degenerate carriers in spin-dependent transport; (4) Formation of large band gap quantum spin Hall state on Si surface. This study reveals the importance of atomic orbital composition in the formation of a topological insulator, and shows promisingly the possible integration of topological insulator technology into Si-based modern electronic devices.

CONTENTS

ABSTRACT . . . . **iii**

LIST OF FIGURES . . . . **vi**

LIST OF TABLES . . . . **ix**

ACKNOWLEDGMENTS . . . . **x**

CHAPTERS

1. INTRODUCTION OF CHARGE DOPING EFFECTS IN SEMICONDUCTOR **1**

1.1 Carrier doping in bulk semiconductor 1
1.2 Charge doping in two-dimensional nanostructure 2
1.3 Charge doping-induced modulation of surface nanostructure growth 6
1.4 Rashba spin-orbit interaction on surface 7
1.5 Surface states in topological insulator 9
1.6 Organization of the dissertation 12
1.7 References 13

2. EFFECTS OF LI DOPING ON H DIFFUSION IN MGH$_2$: A FIRST PRINCIPLES STUDY **15**

2.1 Introduction 15
2.2 Calculation details 16
2.3 Results and discussion 17
2.4 Conclusion 23
2.5 References 25

3. TUNING NUCLEATION DENSITY OF METAL ISLAND WITH CHARGE DOPING OF SUBSTRATE **27**

3.1 Introduction 27
3.2 Calculation details 28
3.3 Results and discussion 29
3.4 Conclusion 35
3.5 References 37

4. STRAIN ENGINEERING OF IDEAL RASHBA STATES ON LAYERED SEMICONDUCTOR SURFACE **39**

4.1 Introduction 39
4.2 Results and discussion 40
4.3 Conclusion 49

4.4 References 49

5. FORMATION OF QUANTUM SPIN HALL STATE ON SI SURFACE AND ENERGY GAP SCALING WITH STRENGTH OF SPIN ORBIT COUPLING 52

5.1 Introduction 52
5.2 Results and discussion 53
5.3 Conclusion 59
5.4 References 61

LIST OF FIGURES

1.1 Schematics of Fermi level positions in intrinsic, electron-doped, and hole-doped semiconductors from the left to the right. CB and VB denote the conduction and valence band, respectively. E_D and E_A denote the corresponding atomic energy levels. . . . 3

1.2 The effects of interadatom interaction on the island density: (a) Schematic of adatom-adatom interaction energy as a function of separation for only direct chemical bonding. (b) Island (each dot) image from kinetic Monte Carlo simulation under (a). (c) Schematic of adatom-adatom interaction energy including beyond nearest-neighbor repulsion. (d) Island image from kinetic Monte Carlo simulation under (c). Adapted from Ref. [20] 8

1.3 2D free electron gas with Rashba SOC: (a) Band structure of 2D free electron gas with Rashba SOC. (b) Spin texture in reciprocal k_x-k_y plane. (c) Datta spin filed transistor. Adapted from Ref. [22]. 10

1.4 Schematic of the band dispersion of Rashba states (on the left) and of surface states of TI (on the right). The arrows represent spin and the bottom and top shared areas are valence band and conduction band, respectively. 11

2.1 Formation energy of Li-dopant in MgH_2: (a) H-poor condition. (b) H-rich condition. The vertical solid and dashed lines indicate the Fermi energy in MgH_2 with and without Li, respectively. E_{Fermi}=0 eV corresponds to the VBM and E_{Fermi} = 3.8 eV corresponds to the CBM. 20

2.2 Binding between V_H^+ and Li_{Mg}^{-1}: (a) The structure of Li-dopant plus H-vacancy with H-vacancy at different positions labeled with number and distance from Li. (b) Interaction energy between V_H^+ and Li_{Mg}^{-1} as a function of their separation distance (in Angstrom). (c) Ratio of the trapped V_H^+ with Li_{Mg}^{-1} to the number of V_H^+, T = 400 K. Green balls are Mg atoms, white balls are H atoms, and orange ball is Li dopant. 22

2.3 Effect of Li presence on V_H diffusion: (a) Illustration of different diffusion path for V_H to diffuse further away from Li site. The arrow indicates diffusion direction; (b) V_H-mediated H-diffusion barrier change with the presence of Li. The purple ball indicates the position of V_H in our calculation. The arrow indicates the diffusion path. 24

3.1 Charge doping effects on Fe adatom properties on graphene substrate: (a) Adsorption energy versus charge doping concentration for Fe adatom at H-site and B-site. (b) Bader charge of Fe adatom at H-site and B-site versus charge doping concentration. (c) diffusion barrier versus charge doping concentration. 31

3.2 Charge doping effect on Fe adatom magnetic properties: (a) Local magnetic moment of Fe adatom of H-site versus charge doping concentration. (b-g) Fe adatom partial density of states with projection to s, p, d orbitals for both spin-up (sup, pup, and dup) and spin-down (sdn, pdn, and ddn) components. 33

3.3 Charge doping effect on Fe interadatom interaction: (a) The six Fe-Fe configurations in increasing order of separation. The configuration is labeled with 1-6 accordingly, relative to the center Fe adatom. (b) Interaction energy between two NN Fe adatoms. (c) Interaction energy as a function of separation beyond NN. 34

3.4 kMC simulated island number density as a function of charge doping concentration for both cases: with adatom-adatom interaction (with E_{ad}) and without adatom-adatom interaction (without E_{ad}). 36

4.1 Atomic structure of Au/InSe(0001): (a) Side view of the (6×6) supercell structure of Au grown on layered InSe(0001) substrate, which is shown with only the top three layers for clarity. (b) Top view of the supercell. α_1 and α_2 represent the surface unit cell vectors. 41

4.2 Band structures of Au/InSe(0001) under different strain cases: (a) strain-free. (b) Compressive strain = -1.2%. (c) Tensile strain = +1.2%. 42

4.3 Rashba states spatial localization: (a) Plane-averaged potential V along z-axis. (b-e) Charge distribution of the Rashba states 1-4, as labeled in Fig. 4.2(b) as as a function of the atomic plane. (f-i) Orbital compositions in the first five atomic planes for the Rashba states 1-4. 44

4.4 Spin polarization textures of the Rashba bands at two iso-energy surfaces of E = 0.0 eV (a-b) and E = -0.12 eV (c-d), respectively. 46

4.5 Spin transistor designed from Au/InSe(0001) nanoribbon: (a) Two-terminal devive setup: the boxes on the left and on the right represent source and drain leads without SOC, respectively. The left lead is ferromagnetic and the right lead is nonmagnetic. The middle dashed-line box represents the channel with Rashba SOC. (b) The band structure of the channel when assuming periodic structure in transport direction (L). The red dashed line shows the Fermi energy position used in the conductance calculation. (c) The spin-up $G_{\uparrow\uparrow}(E_F)$ and spin-down $G_{\uparrow\downarrow}(E_F)$ contributions to the total conductance, as a function of device length (L). 47

5.1 Experimental proposal to grow heavy atoms into hexagonal lattice: (a) Schematic of a two-step approach to fabricate 2D TI by deposition of heavy metal atoms on a patterned H-Si(111) surface. (b, c) The top and side view of the proposed structure, with the surface unit cell vector (a_1, a_2) indicated in (b) and the adsorption length d in (c). (d) The first surface Brillouin zone. 54

5.2 DFT Band structures of heavy metals on patterned Si(111): (a-b) Band structures of Bi and Pb+H-Si(111) without SOC, respectively. The Fermi level is set at zero. The green (yellow) shaded area represents the valence bands (conduction bands) of Si. Band compositions around Fermi level are also indicated. (c-d) Same as (a-c) with SOC. 56

5.3 The edge states from the TI on Si(111): (a) Comparison of band structures for Bi+H-Si(111) calculated by DFT (black lines) and Wannier function method (green circles). (b) The Dirac edge states within the SOC-induced band gap. Scale bar is indicated on the right. (c) The partial DOS projected onto p_x, p_y , and p_z orbitals of Bi, and the total DOS of neighboring Si atoms. (d) Top: The charge density redistribution induced by metal atom surface adsorption for Bi+H-Si(111) (isovalue = 0.02 e/$\mathring{A}^3$), illustrating saturation of Bi p_z orbital. Bottom: Same as Top for the H-saturated freestanding planar Bi lattice. 58

5.4 Energy bands resulting from the four-band model [Eq. (5.1)] as a function of SOC strength (λ) scaled by t (t is the coupling strength between neighboring p_x and p_y orbitals). Fermi energy is set to 0. The SOC-induced energy gaps (ΔE_1, ΔE_2, and ΔE_3) are indicated. The global gap transition from K point to Γ point driven by SOC can be clearly seen. 60

LIST OF TABLES

1.1 Dielectrics used in experiment to tune the charge density of graphene. Here, ionic liquid has the largest capability of charge density modulation. Adapted from Ref. [11]. 5

2.1 The formation energy (ΔE^f) and concentration (C) of relevant H-defects without (a) and with (b) dopant Li, at T = 400 K. 18

ACKNOWLEDGMENTS

First and foremost, I would like to deliver my gratitude to my advisor Professor Feng Liu for his continuous support and inspiration of my research for years. I deeply appreciate the skills and ways of thinking I learned from Professor Feng Liu. I would not have achieved my final dissertation and research publications without these indispensable factors.

I want to express my thank to all the members in Professor Feng Liu's group. I feel very much in debt to all those nice people, who have always been willing to help restlessly and share ideas and solutions along the course of my research and life. I would like to deliver my appreciation to Dr. Zhengfei Wang, Dr. Miao Zhou, Dr. Zheng Liu, Ninghai Su, and Miao Liu for the tremendous amount of suggestions/directions on my research. I want to also thank Peng Yang, Lei Zhang, and Wei Jiang for being friendly and flexible during my time in Utah.

I would like to thank my dissertation committee members, Prof. Ling Zang, Prof. Zak Fang, Prof. Yong-shi Wu, and Prof. Ashutosh Tiwari, for their generosity of spending time and giving critical suggestions/comments on my dissertation.

Particulary, I would like to thank my wife Qin Zhang for her support, love, and understanding during my life in graduate school at the University of Utah. I appreciate the constant support and love from my parents.

CHAPTER 1

INTRODUCTION OF CHARGE DOPING EFFECTS IN SEMICONDUCTOR

1.1 Carrier doping in bulk semiconductor

Carrier (electron or hole) doping of a semiconductor is the most critical step in the development of modern electronic devices, such as p-n junctions and transistors. For undoped semiconductors, the valence band and conduction band are separated by a finite energy gap of E_g. At zero temperature (T), the valence band is fully occupied by electrons and the conduction band is completely empty. At elevated T, the thermal energy excites electrons from the valence band to the conduction band, leaving holes behind in the valence band. This finite concentration of electrons and holes in the conduction and the valence band, respectively, makes the semiconductor begin to be conductive. However, the concentration of the intrinsic carriers under thermal excitation is very small, being proportional to $\exp(-E_g/2k_BT)$, where k_B is the Boltzmann constant, k_BT is the thermal energy, which is 0.026 eV at room temperature (RT). For the case of Si, with E_g of 1.12 eV, the intrinsic carrier concentration is only $\sim 10^{10}/cm^3$ at RT, far less than the typical number density of constituent atoms: $\sim 10^{24}/cm^3$. Therefore, an undoped semiconductor is essentially insulating [1].

In order to have a higher concentration of carriers, doping of the intrinsic semiconductor by foreign atoms with a different number of valence electrons from the host atoms was adopted to introduce additional electrons into the conduction band or holes into the valence band. Doping of B and P are the usual choices to introduce holes and electrons in Si, respectively. The highest atomic energy levels of B and P are quite close (only 0.045 eV) to the valence band and conduction band edge, respectively, so that they are easy to thermally ionize at RT, by accepting electrons from the valence band and donating electrons to the conduction band, respectively. Apart from the carrier concentration tuning by external dopants, another important consequence from the ionization process is that Fermi energy (E_F) is shifted closer to the valence band under hole-doping (p-doping) or the conduction band under electron doping (n-doping) (see the schematic of Fermi energy shifting in Fig. 1.1). This controllable change of Fermi energy will also affect the concentration of the charged intrinsic defects existing in a semiconductor, such as vacancy and antisite, because the formation energy of charged defect depends critically on the Fermi energy [2]. There have been intensive studies of defect concentration as a function of Fermi energy in semiconductors for decades. A similar principle was applied to one of our projects: effect of Li doping on H-vacancy diffusion for hydrogen storage [3].

1.2 Charge doping in two-dimensional nanostructure

For semiconductors with lower dimensions, such as the surface, ultrathin film, and molecular overlayer on the substrate, there exist various methods of doping other than chemical substitutional doping as conventionally used in bulk semiconductors. Because of the small thickness of the surface layer, the charge transfer from/to the substrate intrinsically dopes the overlayer. In another version of carrier doping by the substrate, an ultrathin insulating film of only a few atomic layers is sandwiched between the underlying metallic substrate and the topmost layer of interest; the charge transfer then occurs indirectly through quantum tunneling over the insulating film from the metal substrate to the overlayer film. With different thickness of sandwiched film, the charge tunneling can be tuned and the doping concentration is thus controllable by adjusting the thickness of the middle insulating film. Such tunable film doping concentration through the substrate can also realized by different substrate and/or surface/sub-surface doping, indirectly providing the top-layer thin film with varying carrier concentration. It is also common that in surface adsorption of atoms or molecules, the charge transfer can occur between the ad-species (such as organic ad-molecules and metal adatoms) and the underneath thin film, thereby achieving the charge doping effect. An additional method of tuning surface carrier concentration is electric field effect, where the charge is separated from the thin film to the top metallic gate or vice versa with a dielectric material in-between. By varying gate voltage and dielectric materials of a different dielectric constant, the surface carrier concentration can be varied over a wide range ($> 10^{12}/cm^2$).

For pristine graphene, the electron density of states at Fermi energy is zero. Therefore, finding effective doping methods, which can control the carrier type and concentration, is of essential importance for the application of graphene-based electronic devices and the study of new physics from the linear energy dispersion. Structurally, graphene has strong in-plane covalent sp^2 bonding, which is responsible for its superior mechanical strength.

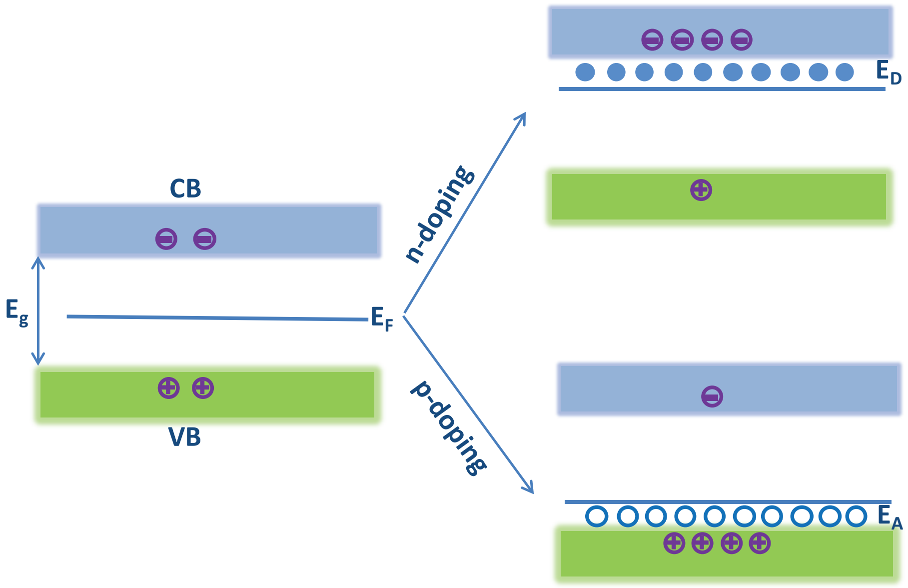

Figure 1.1. Schematics of Fermi level positions in intrinsic, electron-doped, and hole-doped semiconductors from the left to the right. CB and VB denote the conduction and valence band, respectively. E_D and E_A denote the corresponding atomic energy levels.

Breaking a strong C-C bond requires high energy cost, so it has been difficult to use foreign atoms (for example, B or N) to substitute C atoms in order to dope graphene experimentally during the epitaxial growth of graphene. To overcome the difficulty of substitutional doping, there is some experimental progress made so far: (1) N^+ ion irradiation of graphene with NH_3 atmosphere of annealing. The working mechanism is that first uniform C vacancies are generated after N+ irradiation. Then in the atmosphere of NH_3, N is introduced into the sites of carbon vacancies [4]; (2) Chemical vapor deposition (CVD) using CH_4 and NH_3 to be the host carbon source and N dopants, respectively [5]; (3) Arc discharge method in the atmosphere of either B_2H_6 or NH_3, respectively, for B-doped and N-doped graphene [6]. Graphene π bonds are much weaker due to smaller orbital overlap than sp^2 bonds. Thus, graphene is anticipated to be a good platform to support reactive atoms or molecules adsorbed on it. The possible charge transfer between adsorbate and graphene will consequently induce electron or hole doping in graphene. On the experimental side, Potassium adatom is very often adopted to n-type dope graphene [7] and Bismuth adatom to p-type dope graphene [8]; small organic molecules are also shown to dope graphene through adsorption. On the theoretical side, metal adatoms (free electron like simple metals, transition metals, noble metals, and rare earth metals) are studied for doping graphene and the interactions of metal adatoms on graphene are calculated in Ref. [9], showing a variety of charge transfer behaviors.

Electric gating is commonly used to adjust the charge carrier type and concentration of graphene [10]. In so doing, Fermi energy of graphene can be pushed up or down away from the Dirac point. For most conventional dielectrics, the charge tunability is quantified by the linear relationship with gate voltage V_g: $n = \alpha^* V_g$, where n is how much charge per unit area can be added (electrons) or removed (holes) and α is a coefficient proportional to static dielectric constant κ. The maximum gate voltage which can be applied to a dielectric material is limited by the value of electric breakdown. Therefore, in order to achieve a wider range of charge doping, a dielectric material with sufficiently large κ is desired. Experimentally, researchers tried several dielectric materials as listed in Table 1.1 to modulate the charge density in graphene. All these dielectric materials are called linear dielectrics due to the linear relationship between their dielectric constant and the gate voltage. To further enhance the charge tunability, ferroelectric materials are also used as gate dielectrics due to its large dielectric constant and nonlinear behavior [11]. The maximum charge doping can be larger than $10^{14}/cm^2$.

Table 1.1. Dielectrics used in experiment to tune the charge density of graphene. Here, ionic liquid has the largest capability of charge density modulation. Adapted from Ref. [11].

Top Gate dielectric	Dielectric constant ε /capacitance C	Maximum charge density n modulation achieved
Cross linked PMMA	$\varepsilon \sim 4.5$	$n \sim 5 \times 10^{12}/cm^2$
ALD-deposited Al_2O_3	$\varepsilon \sim 6$	$n \sim 5 \times 10^{12}/cm^2$
Hydrogen silsesquioxane(HSQ) +ALD-deposited HfO_2	$\varepsilon \sim 12$	$n \sim 4 \times 10^{12}/cm^2$
Organic seed layer +ALD-deposited HfO_2	$\varepsilon \sim 10$	–
Electron-beam evaporated SiO_2	$\varepsilon \sim 4$	$n \sim 1.1 \times 10^{13}/cm^2$
Air-bridge	$\varepsilon \sim 1$	$n \sim 4.0 \times 10^{12}/cm^2$
Polymer electrolyte (polyethylene oxide+$LiClO_4$)	$C = 1\mu F/cm^2$	$n \sim 5.0 \times 10^{13}/cm^2$
Polymer electrolyte (polyethylene oxide+$KClO_4$)	$C = 7.4\mu F/cm^2$	$n \sim 4.0 \times 10^{13}/cm^2$
Ionic liquid	$C = 120\mu F/cm^2$	$n \sim 8.0 \times 10^{14}/cm^2$

1.3 Charge doping-induced modulation of surface nanostructure growth

It has been shown that surface charge doping can tune the properties of not only the surface itself, but also the surface ad-species and their nucleation and growth into an overlayer. The surface charge effect by adsorption of alkali metal atoms or organic molecules has long been identified as responsible for the surface reconstruction of noble metals, such as Ag (110) and Au (111) [12]. The physical mechanism is that under external charge doping, the reconstructed structure is energetically favorable to the clean surface counterpart. It has been recently reported that surface charge doping can also be used to enhance the mechanical strength [13] and superconductivity of graphene [14]. Also the magnetic anisotropy was predicted to be tunable in a metallic multilayer (e.g., Pt/Fe/Pt(001)) by surface charge doping [15]. On the other hand, nucleation and growth of the ad-species overlayer on the surface may also be affected by surface charge doping. For example, the tunable negative charge state of Au adatom on the ultrathin MgO film on Ag(001) forms by adjusting the thickness of MgO film (1-5 monolayers), which results in thickness-dependent indirect charge-transfer from the metallic Ag(001) substrate [16]. In contrast, the charge state of Au adatom can be changed to be positive by choosing a substrate of Pt(111)-supported FeO ultrathin film (1 bilayer of Fe-O) [17]. Although the two different choices of substrate lead to negative and positive charge states of Au adatoms on the oxide film, the final ordered structures formed are very similar, because of the similar resulting Coulomb repulsion between adatoms in both situations.

As pointed out in Ref. [17], MgO/Ag(001) has a lower work function FeO/Pt(111), as the latter has an exceptionally high work function. This causes the electron to flow from MgO/Ag(001) to Au adatoms but oppositely from Au to FeO/Pt(111). An important implication from this difference in the two systems is that the adatom charge states can be tuned by work function control of the substrate.

Other than the different charge states of the adatom, an additional consequence it may have is that the adatom adsorption energy can be doping-dependent, because of different charge transfer and orbital hybridization between the adatom and substrate. Another important parameter in determining the final growth morphology is the diffusion barrier and nucleation density in the initial stage of film growth. Because the diffusion barrier is the energy difference between adsorption energies at the transition state and stable adsorption state, it shall be also affected by surface charge doping. Lastly, as already indicated by the experiment in Ref. [17], the adatom-adatom interaction should be modified because of the tunable charge-state, which gives rise to a different effective adatom-adatom electrostatic interaction under different charge doping condition.

In the field of film growth, mean-field nucleation theory is usually used to extract the diffusion barrier from scanning tunneling microscope (STM) image data of island number density N$_x$. This theory only includes the short-ranged nearest-neighbor chemical interaction. With continuing deposition of adatoms onto the substrate, N$_x$ eventually attains a steady-state when adatom diffusion length becomes comparable to island separation. Experimentally, this usually occurs when the surface coverage is under 10%. Formally, at the steady state [18] $N_x = C\eta(\theta, i)(\frac{F}{D})^{\frac{i}{i+2}} \exp(\frac{E_i}{k_b T})^{\frac{1}{i+2}}$, where F is the depositon flux, i is the critical island size, and D is adatom diffusion rate that can be related to diffusion barrier E$_d$ as $D = \nu_0 \exp(-\frac{E_d}{k_b T})$. However, with inclusion of adatom-adatom repulsion, such as the electrostatic interaction of charged adatoms, N$_x$ can hardly reach a steady state before a continuous film forms. The repulsion provides an additional energy barrier compared to the case without adatom-adatom repulsion, which reduces the probability of a jumping adatom to attach to an existing island for it to grow bigger, but increases the probability of a jumping adatom to find another jumping adatom to nucleate a new island of smaller size. Thus, N$_x$ is expected to increase significantly if this additional repulsion energy is comparable to the diffusion barrier E$_d$, which is small in weakly corrugated system, such as Al/Al(111) [19] and Cu/Cu(111) [20]. On the other hand, if adatom-adatom interaction energy is far smaller than the diffusion barrier [21], it is still quite suitable to describe the island density vs. surface coverage using mean-field nucleation theory. To illustrate these two cases, the schematics of the adatom-adatom interaction energy vs. separation and N$_x$ are shown in Fig. 1.2.

1.4 Rashba spin-orbit interaction on surface

Rashba spin-orbit coupling (RSOC) was a relativistic effect of electron at interface or surface with nonzero electric potential gradient or electric field. Solving the RSOC Hamiltonian of $H = \alpha(z \times k) \bullet \sigma$ of 2D free-electron model in perpendicular electric field, the band dispersion and spin texture can be obtained as in Fig. 1.3 (a-b): first, at each +k point, the energy degeneracy of spin-up and spin-down states is lifted. However, because of time reversal symmetry of RSOC Hamiltonian, the spin configuration of the two corresponding states at -k is exactly opposite to those at +k and the net magnetization remains zero. Second, the spin polarization completely lies in-plane with zero out-of-plane component, and it is perpendicular to k. These two observations can be easily deduced from the k-dependent effective "magnetic field" of $\alpha(z \times k)$ in RSOC Hamiltonian, which is

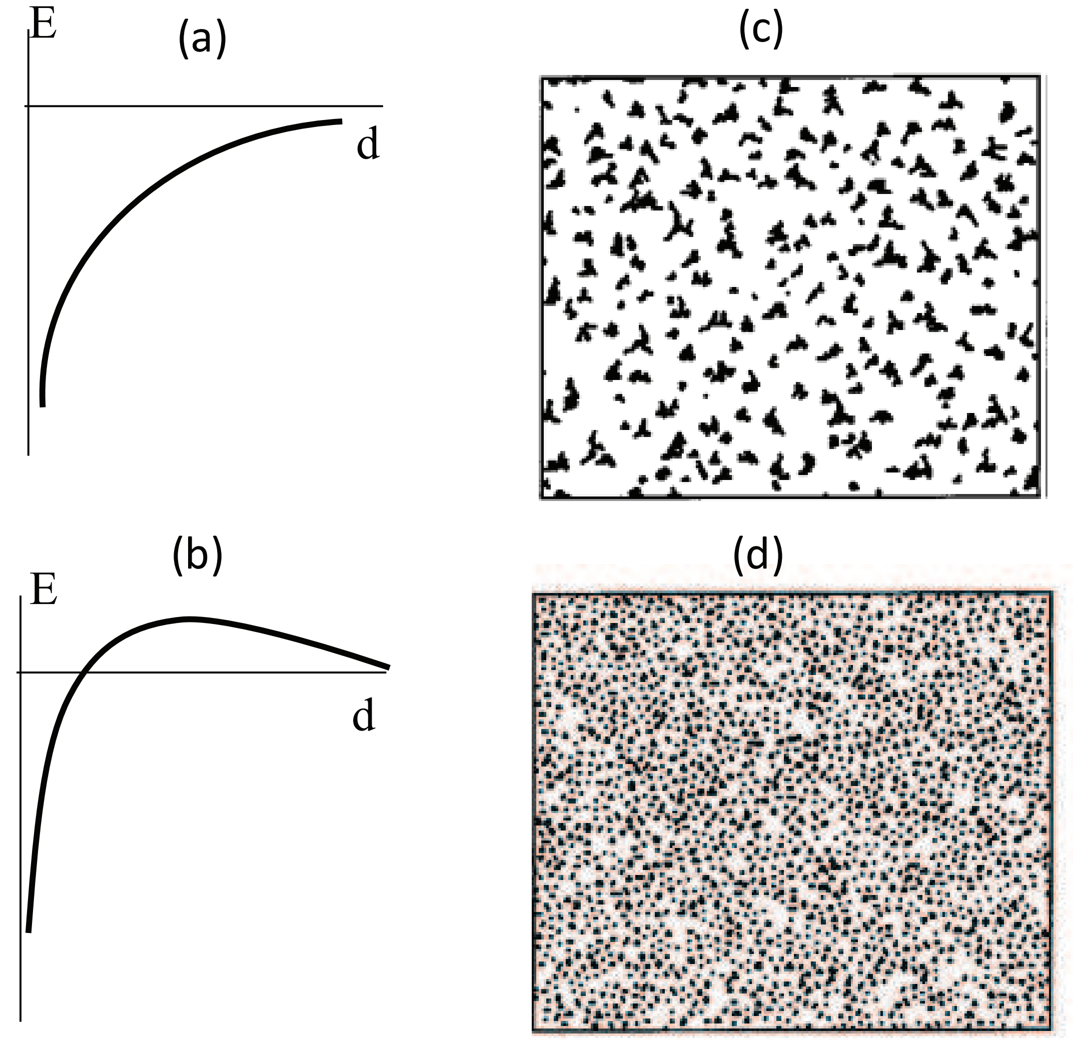

Figure 1.2. The effects of interadatom interaction on the island density: (a) Schematic of adatom-adatom interaction energy as a function of separation for only direct chemical bonding. (b) Island (each dot) image from kinetic Monte Carlo simulation under (a). (c) Schematic of adatom-adatom interaction energy including beyond nearest-neighbor repulsion. (d) Island image from kinetic Monte Carlo simulation under (c). Adapted from Ref. [20]

in-plane and perpendicular to k. The two split states are ones with spin polarization along the direction of the effective "magnetic field" and the other one with spin polarization opposite to the direction of the effective "magnetic field".

Earlier in 1990, Datta et al [22] proposed a spin field effect transistor shown in Fig. 1.3 (c) based on 2D electron gas in SOC. The physical mechanism was presented as following: if we inject spin-up polarized electrons into the free electron conducting channel with RSOC, say, along y direction, then the wavefunction in the channel is:

$$\psi(x) = \begin{pmatrix} 1 \\ 1 \end{pmatrix} \times \exp(ik_1 y) + \begin{pmatrix} 1 \\ -1 \end{pmatrix} \times \exp(ik_2 y). \tag{1.1}$$

At the end of the channel (of length L), the probability of detecting spin-up electron is $p_\uparrow = \cos^2 \frac{(k_2-k_1)L}{2}$ and the probability of detecting spin-down electron is $p_\uparrow = \sin^2 \frac{(k_2-k_1)L}{2}$, where $k_2 - k_1 = \frac{2m}{\hbar^2}\alpha\ L$. Therefore, if different gate voltage is applied (which changes α), the spin-polarized current detected will be different and becomes tunable with gate voltage. The spin precession characteristic length is $L_{so} = (\frac{\pi}{\alpha})(\frac{\hbar^2}{2m})$, at which a spin-up polarization is entirely flipped into a spin-down polarization [23].

Realizing that RSOC is the mechanism for spin-flip, a simpler way to understand the spin-precession is that when channel length is very short, spin-up polarization at the detector is almost unchanged. With longer channel length, spin-up polarization experiences large rotation, becoming spin-down polarization. With even longer channel, the spin-down polarization starts to rotate back towards the spin-up polarization. Because L_{so} is inversely proportional to α, long channel length is required in order to have a π rotation of spin-polarzation if α is small, such as in 2D electron gas formed at the interface of semiconductor heterojunction. In order to reduce the channel length, a large α is needed from interface or surface with larger atomic SOC and potential gradient [24].

1.5 Surface states in topological insulator

Different from the conventional band insulator, the topological insulator (TI) is a new phase of quantum matter, which possesses gapless surface states or edge states protected by time-reversal symmetry [25]. There have been many TIs both predicted theoretically and confirmed experimentally, such as Bi_2Se_3 and Bi_2Te_3 with band-gap of 0.35 eV and 0.15 eV, respectively. Fig. 1.4 shows the schematic of surface band dispersion of TI (on the right) and of the Rashba surface states (on the left). Similar to Rashba states, the spin splitting of bands also exists at each k-point in TI. A difference as indicated by the red arrows is that there is only one Kramer pair (spin up,+k; spin down, -k) in TI surface bands with opposite spin polarizations; hence, the back-scattering from (spin-up, +k) to

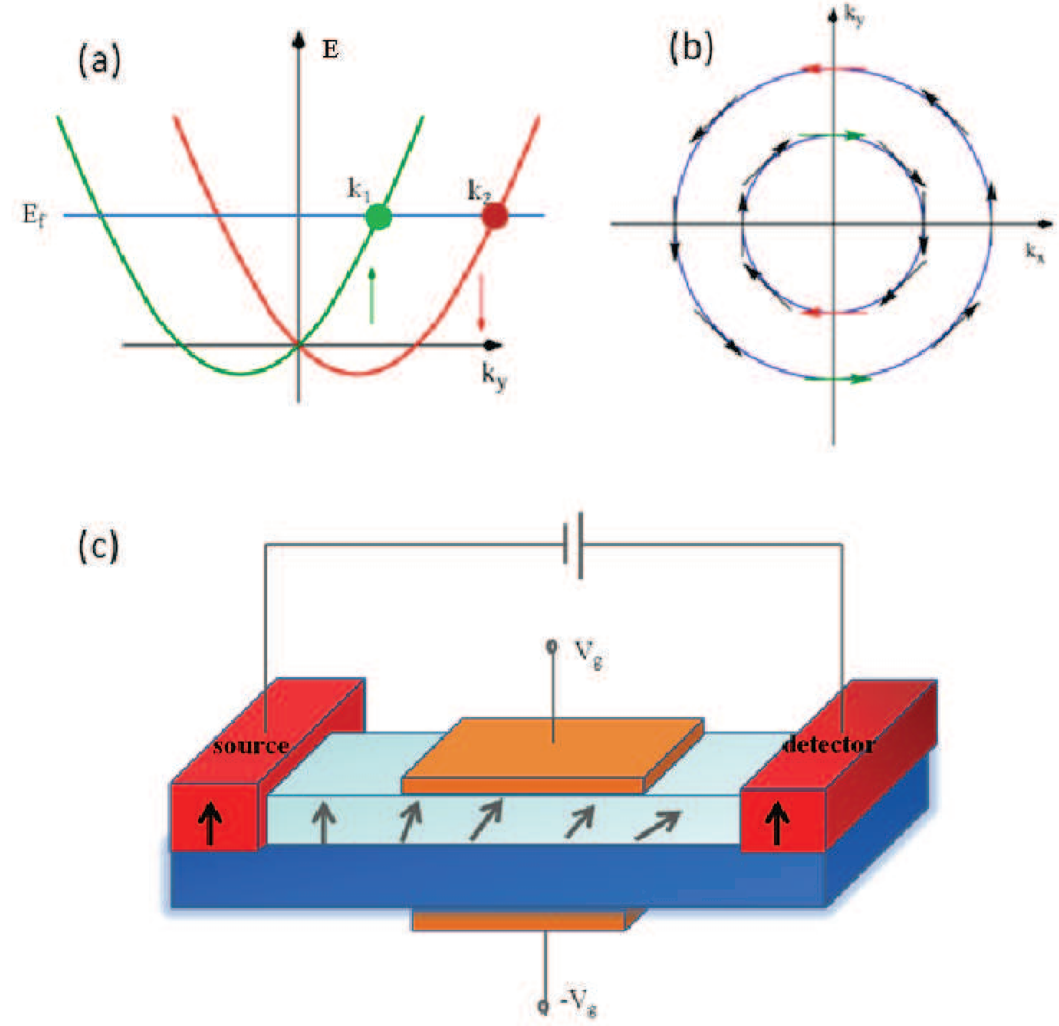

Figure 1.3. 2D free electron gas with Rashba SOC: (a) Band structure of 2D free electron gas with Rashba SOC. (b) Spin texture in reciprocal k$_x$-k$_y$ plane. (c) Datta spin filed transistor. Adapted from Ref. [22].

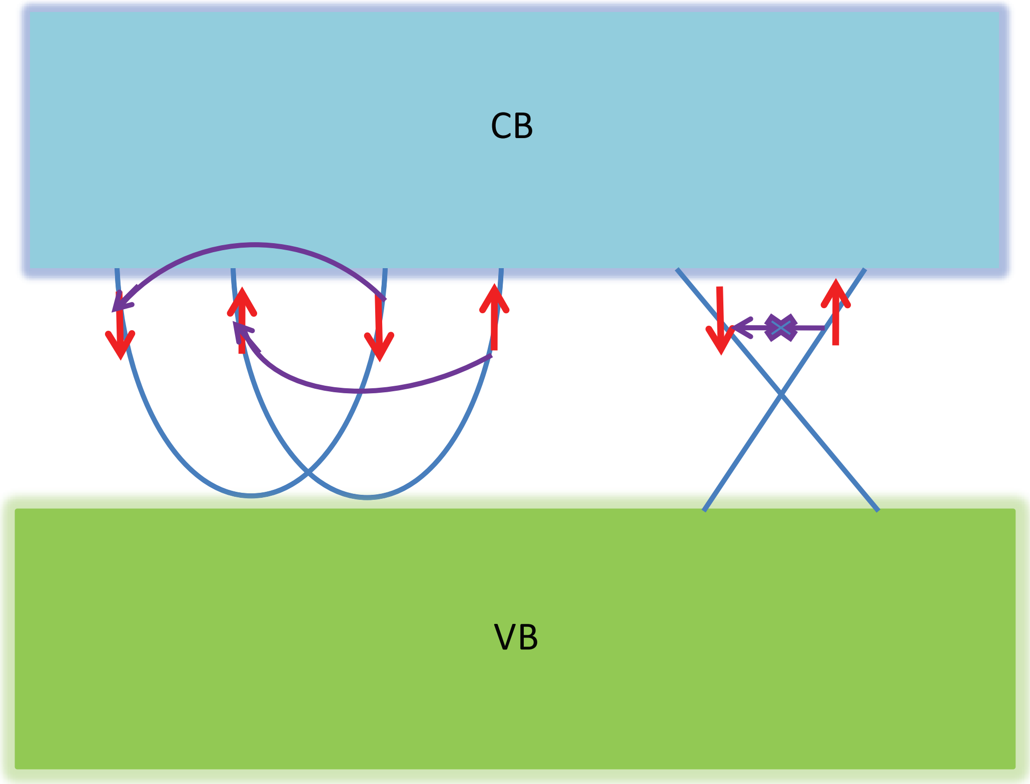

Figure 1.4. Schematic of the band dispersion of Rashba states (on the left) and of surface states of TI (on the right). The arrows represent spin and the bottom and top shared areas are valence band and conduction band, respectively.

(spin-down, -k) is forbidden; but there are two Kramer pairs (spin up, +k_1; spin down, -k_1; spin down, +k_2; spin up, -k_2) in Rashba surface bands, so that the back-scattering such as (spin up, +k_1) to (spin up, -k_2) can occur. Because of the unique forbidden back-scattering property in its surface electronic states, TI has attracted tremendous research interest in the last decade. However, the band gap formation in TI is generally a SOC mechanism rather than from the charge localization mechanism as in the band insulator, so that its band-gap has been found so far very small with the largest band gap of 0.35 eV of Bi_2Se_3 among experimentally confirmed TIs. The ideal TI should have even larger band gap and is less vulnerable to the substrate, in particular for the thin film topological insulator. Together with the Rashba surface states, two of the goals of this dissertation are to explore approaches to realize ideal Rashba surface states and topological surface states on large band gap semiconductor surfaces.

1.6 Organization of the dissertation

In this thesis, atomistic simulation techniques, including density functional theory, kinetic Monte Carlo, nonequilibrium Green's function method, and tight binding method, were employed, which will be discussed in Chapter 2, 3, and 4, respectively.

In the second chapter, charge effects on the formation energy and the diffusion energy barrier of H vacancy defect were studied in bulk MgH_2 under light Li doping for improved hydrogen storage application. Particularly, the interaction between defect and dopant is included, which is mostly neglected in previous work.

In the third chapter, surface charge doping was proposed to be an effective way to tune the number density of the metal island grown on the semiconductor substrate. Using Fe growth on graphene as an example, Fe adatom adsorption energy, charge transfer, diffusion barrier, and electronic static interaction were investigated. Subsequently, the effect of charge doping on the metal island density was also revealed.

In the fourth chapter, following the idea of tunable adatom-surface interaction, the heavy Au adatom with large SOC was chosen to be grown epitaxally on the large band gap InSe(0001) triagonal surface. The clean Rashba spin splitting bands were found to lie completely in the bulk band gap of the substrate. The mechanism of the Rashba band formation was analyzed and the nearly free-electron like spin texture was shown to appear in this system. Additionally, the modulation of spin polarized current was demonstrated by calculating the conductance as a function of channel length.

In the fifth chapter, a new route to the formation of the topological insulator by depositing heavy atoms on Si(111) surfaces was explored. The physical mechanism of orbital filtering effect was uncovered to provide a general picture for the creation of the topological insulator from an orbital filtering point of view.

1.7 References

[1] S. M. Sze, Physics of Semiconductor Devices, chapter 1, Wiley, New York, 1981.

[2] S. B. Zhang and J. E. Northrup, Phys. Rev. Lett. 67, 2339 (1991).

[3] Wenmei Ming, Zhigang Zak Fang and Feng Liu, J. Appl. Phys. 114, 243502 (2013).

[4] B. Guo et al., Nano Lett. 10, 4975 (2010).

[5] D. Wei et al., Nano Lett. 9, 1752 (2009).

[6] L. S. Panchokarla et al., Adv. Matter. 21, 4726 (2009).

[7] A. Bostwick, T. Ohta, T. Seyller, K. Horn and E. Rotenberg, Nature. Phys. **3**, 36 (2007).

[8] I. Gierz, C. Riedl, U. Starke, C. R. Ast and K. Kern, Nano Lett. **8**, 4603 (2008).

[9] K. T. Chan, J. B. Neaton and M. L. Cohen, Phys. Rev. B **77**, 235430 (2008).

[10] K. S. Novoselov, A. K. Geim, S. V. Morozov, D. Jiang, Y. Zhang, S. V. Dubonos, I. V. Grigorieva, A. A. Firsov, Science **306**, 666 (2004).

[11] M. F. Craciun, et al., arXiv 1101.4383; Y. Zheng, G. X. Ni, C. T. Toh, C. Y. Tan, K. Yao and B. Ozyilmaz, Phys. Rev. Lett. **105**, 166602 (2010).

[12] C. L. Fu and K. M. Ho, Phys. Rev. Lett. **63**, 1617 (1989).

[13] C. Si, W. Duan, Z. Liu, and F. Liu, Phys. Rev. Lett. **109**, 226802 (2012).

[14] C. Si, W. Duan, Z. Liu, and F. Liu, Phys. Rev. Lett. **111**, 196802 (2013).

[15] P. Ruiz-Diaz, T. R. Dasa and V. S. Stepanyuk, Phys. Rev. Lett. **110**, 267203 (2013).

[16] Martin Sterrer et al., Phys. Rev. Lett. **98**, 096107 (2007).

[17] Livia Giordano et al., Phys. Rev. Lett. **101**, 026102 (2008).

[18] H. Brune, Surf. Sci. Rep. **31**, 125 (1998).

[19] A. Bogicevic, S. Ovesson, P. Hyldgaard, B. I. Lundqvist, H. Brune and D. R. Jennision, Phys. Rev. Lett. **85**, 1910 (2000).

[20] S. Ovesson, Phys. Rev. Lett. **88**, 116102 (2002).

[21] J. A. Venables, G. D. T Spiller and M. Hanbucken, Rep. Prog. Phys. **47**, 399 (1984).

[22] Supriyo Datta and Biswajit Das, Appl. Phys. Lett. **56**, 665 (1990).

[23] Francisco Mireles and George Kirczenow, Phy. Rev. B, **64**, 024426 (2001).

[24] L. Petersena and P. Hedegard, Surf. Sci. 459, **49** (2000).

[24] Haijun Zhang, Chao-Xing Liu, Xiao-Liang Qi, Xi Dai, Zhong Fang and Shou-Cheng Zhang, Nat. Phys. **5**, 438 (2009)

CHAPTER 2

EFFECTS OF LI DOPING ON H DIFFUSION IN MGH$_2$: A FIRST PRINCIPLES STUDY

2.1 Introduction

Light metal hydride MgH$_2$ is one of the most promising hydrogen-storage materials for on-board clean fuel application, because it has both high gravimetric ($7.7wt\%$) and volumetric densities ($6.7\times 10^{22}H/cm^3$) [1]. However, their dehydrogenation process is too slow to be practically useful, and for bulk materials, 300 K above room temperature is required to obtain an equilibrium H$_2$ pressure of 1 bar [1-4]. Such poor dehydrogenation kinetics is primarily due to the strong ionic bonding between Mg and H and large enthalpy of formation of MgH$_2$ ($\sim$ 75KJ/molH$_2$), as evidenced by both experiments [5-7] and first principles calculations [8-9]. Various attempts have been made to help facilitate the dehydrogenation process. For example, to improve the kinetics, ball milling processing [10-11] has been used to shorten the diffusion length, doping of transition metals [10-12] were adopted to reduce the strength of the H-Mg bond, and applying tensile stress was tried to weaken the Mg-H stability [2,13].

On the other hand, doping has been known to enhance H diffusion in metal hydrides, which is usually mediated by H vacancy, by inducing a higher concentration of H-vacancy [14-19]. For example, Van de Walle *et al.* recognized that in certain charged states, Zr(Ti) can enhance the dehydrogenation kinetics of NaAlH$_4$ [14], because the formation energy of H-vacancy is decreased upon doping. In particular, when the H-vacancy is charged, its formation energy depends on the position of Fermi energy; conversely, selective doping of the hydride with dopants that take different charged states will tune the Fermi energy with respect to the dopant-free system. Furthermore, the shift of Fermi energy can result in a decrease of H-vacancy formation energy depending on the sign of the H-vacancy charge state. Consequently, the concentration of H-vacancy will increase to enhance the vacancy-mediated H diffusion.

In this work, we investigated the effects of Li doping on H diffusion in MgH_2. One important reason that we chose Li is because it is a lighter metal than Mg, so that it will not degrade the high H gravimetric density. We focused on the effects of the charge state of Li dopant and H-vacancy, as recognized before in other systems [14], but also went beyond the previous works by taking into account the effects of interaction between the charged dopants and defects. In many previous studies of the charged-dopant-enhanced H diffusion [14-19], it implicitly assumed no interaction between the dopant and defect. This might be true in the limit of low doping concentration and weak dopant-defect interaction, but unlikely at high doping concentration. Especially, if there is an attractive dopant-defect interaction, such as the binding between the Li-dopant and H-vacancy in MgH_2 as shown by Smith *et al.* [20], the dopant may immobilize the H-vacancy, counteracting the enhancement effect of H-vacancy on H diffusion.

Therefore, by taking into account the binding between Li and H-vacancy and its dependence on the charge states of Li and H-vacancy, we have systematically studied the effects of Li doping on H diffusion in MgH_2 as a function of Li concentration. We have determined the favored charge states of Li by calculating its formation energy as a function of Fermi energy, the equilibrium concentration of H-vacancies by calculating the H-vacancy formation energy as a function of Li doping concentration, and the percentage of immobilized H-vacancies by calculating the binding energies between H-vacancy and Li-dopant. We have also calculated the diffusion barrier of H-vacancy in the presence of Li-dopant.

2.2 Calculation details

Our first principles calculations based on density functional theory (DFT) were conducted using projector augment wave pseudopotential (PAW) [21] with the generalized gradient approximation (GGA) [22] to the exchange-correlation functional, as implemented in the VASP package [23]. Supercell technique was used to calculate the formation energy of defects and dopants, interaction energy, and diffusion barrier. We used a supercell comprised of $3\times3\times4$ primitive MgH_2 rutile unit cells with the dimensions of $13.481\times13.481\times12.012\mathring{A}^3$. 400 eV energy cutoff and $2 \times 2 \times 2$ k-mesh were used for wavefunction expansion and k-space integration, respectively. All the structures were relaxed in terms of internal atomic coordinates using conjugate gradient method until the force exerted on each atom was smaller than $0.005eV/\mathring{A}^3$. The charged system was simulated by adding to or removing from the system electrons with a compensating uniform opposite charge background. Diffusion barrier was calculated using the nudged elastic band method [24].

The formation energy $E^f(X^q)$ of defect or dopant (X) with charge q was computed according to Ref. [25]:

$$\Delta E^f(X^q) = E_{tot}(X^q) - E_{tot}(bulk) - \sum_i n_i\mu_i$$
$$+q(E_F + E_\nu + \Delta V) \qquad (2.1)$$

where $E_{tot}(bulk)$ and $E_{tot}(X^q)$ are the total energies of supercell for pure MgH_2 and for MgH_2 containing defect or dopant (X^q), respectively. E_ν is chosen to be the valence band maximum (VBM) energy. E_F is the Fermi energy with respect to E_ν. ΔV is additional electrostatic energy alignment due to different energy references between the defect-containing structure and defect-free structure. i denotes H-defect or dopant Li and n_i is the number of species i in the supercell. μ_i is the chemical potential of species i. In low concentration limit, the equilibrium defect concentration can be related to the formation energy using:

$$C = N\exp(-\Delta E^f/k_BT) \qquad (2.2)$$

N is the number of sites that can be occupied by defect, k_B is the Boltzman constant, and T is temperature in K.

For the chemical potential μ_i, the externally added dopant Li is assumed to have its bulk chemical potential $E_{Li}(bulk)$. The chemical potential of H, μ_H is in-between $\frac{1}{2}E(H_2) + \frac{1}{2}\Delta H_f(MgH_2)$ (H-poor condition) and $\frac{1}{2}E(H_2)$ (H-rich condition), considering thermodynamic equilibrium between MgH_2, Mg, and H_2. $\Delta H_f(MgH_2)$ is the enthalpy of formation of MgH_2, E(H_2) is the energy of the hydrogen molecule at 0 K. Similarily, the chemical potential of Mg is in-between E(bulk Mg) and E(bulk Mg)+ΔH_f(MgH_2). We specifically considered two extreme cases: H-poor condition and H-rich condition.

2.3 Results and discussion

First we calculated the formation energy of native defects: H-vacancy (V_H with charge -1, 0, +1) and interstitial H (H_i with charge -1, 0, +1). The preferred defects are V_H^{+1} and V_H^{-1} in H-poor condition, and V_H^{+1} and H_i^{-1} in H-rich condition, respectively. Charge neutrality condition requires Fermi-energy to be 2.85 eV and 2.65 eV for the H-poor condition and H-poor condition, respectively. These results are in good agreement with those for MgH_2 in Ref. [17]. In Table 2.1 we give an estimate of the concentration for the favored H-defects from equation (2.2).

In order to study how the formation energies of the H-related defects are affected by Li doping, we then calculated the formation energy for both substitutional Li configuration

Table 2.1. The formation energy (ΔE^f) and concentration (C) of relevant H-defects without (a) and with (b) dopant Li, at T = 400 K.

	H-poor		H-rich	
	V_H^+	V_H^-	V_H^+	H_i^-
Δ E^f(eV)^a	1.225	1.225	1.358	1.358
C($/cm^3$)^a	2.5×10^7	2.5×10^7	5.3×10^5	5.3×10^5
Δ E^f(eV)^b	0.975	1.475	0.968	1.748
C($/cm^3$)^b	3.5×10^{10}	1.772×10^4	4.13×10^{10}	6.5

(Li_{Mg}) and interstitial Li configuration (Li_i) in the (-1, 0, +1) charge states. As shown in Fig. 2.1 for both H-poor and H-rich conditions, Li_{Mg}^{-1} is more stable than Li_{Mg}^{0} and Li_{Mg}^{+1} in almost the whole range of Fermi energy in the gap except very close to the VBM, while Li_i^{+1} is more stable than the other two charge states in almost the whole range of Fermi energy in the gap except very close to the conduction band minimum (CBM). This indicates that the defect level remains close to the VBM and CBM for Li_{Mg} and Li_i, respectively (see Ref. [26] for similar behavior of native defects in anatase $\mathrm{TiO_2}$). Under the charge-neutrality condition, the Fermi energy of the Li-doped system (vertical solid lines) is shifted to the left by 0.25 eV (Fig. 2.1(a)) and 0.39 eV (Fig. 2.1(b)) with respect to the Fermi energy of the undoped system (vertical dashed lines) for the H-poor and H-rich condition, respectively, assuming the concentration of dopant Li is much higher than that of H-defects so that the Li_i^{+1} and Li_{Mg}^{-1} are the dominant charged dopants to maintain the charge-neutrality condiction. The Fermi energy in both situations is deep inside the band gap. Thus, the thermally excited free carriers in both the valence and conduction band are negligible. The consequence of the shift of Fermi energy is that the formation energy of V_H^{+1} is reduced by 0.25 eV and 0.39 eV under the H-poor and H-rich condition, respectively, according to Eq. (1). And the opposite effect happens to V_H^{-1} and H_i^{-1}: their formation energy is increased by 0.25 eV and 0.39 eV, respectively. As shown in Table 2.1, at 400K the concentration of V_H^{+1} in the Li-doped system is 1.40×10^3 and 8.12×10^4 times larger than that in the undoped system under the H-poor and H-rich condition, respectively. On the contrary, the concentration of H_i^{-1} in the Li-doped system is $\sim10^5$ and $\sim 5\times10^7$ times lower than that in the undoped system under the H-poor and H-rich condition, respectively.

A previous calculation [18] showed that in the undoped $\mathrm{MgH_2}$, the diffusion barrier of V_H^{+1} is 0.25 eV smaller than that of V_H^{-1} under the H-poor condition, and the diffusion barrier of V_H^{+1} is 0.36 eV higher than that of H_i^{-1} under the H-rich condition. This means that without Li doping, the V_H^{+1} is the dominant diffusing species under the H-poor condition, while the H_i^{-1} is the dominant diffusing species under the H-rich condition. Our calculations show that upon Li doping, the formation energy of V_H^{+1} is decreased by 0.25 eV under that H-poor condition, while that of H_i^{-1} is increased by 0.39 eV under H-rich condition. Because the H-related defect diffusion is determined by the activation barrier, which is the sum of the diffusion barrier and the formation energy. The V_H^{+1} remains the dominant diffusing species under the H-poor condition because its formation energy is decreased, leading to a lower activation barrier. In contrast, the H_i^{-1} becomes the less favorable diffusing species under the H-rich condition because its formation energy is

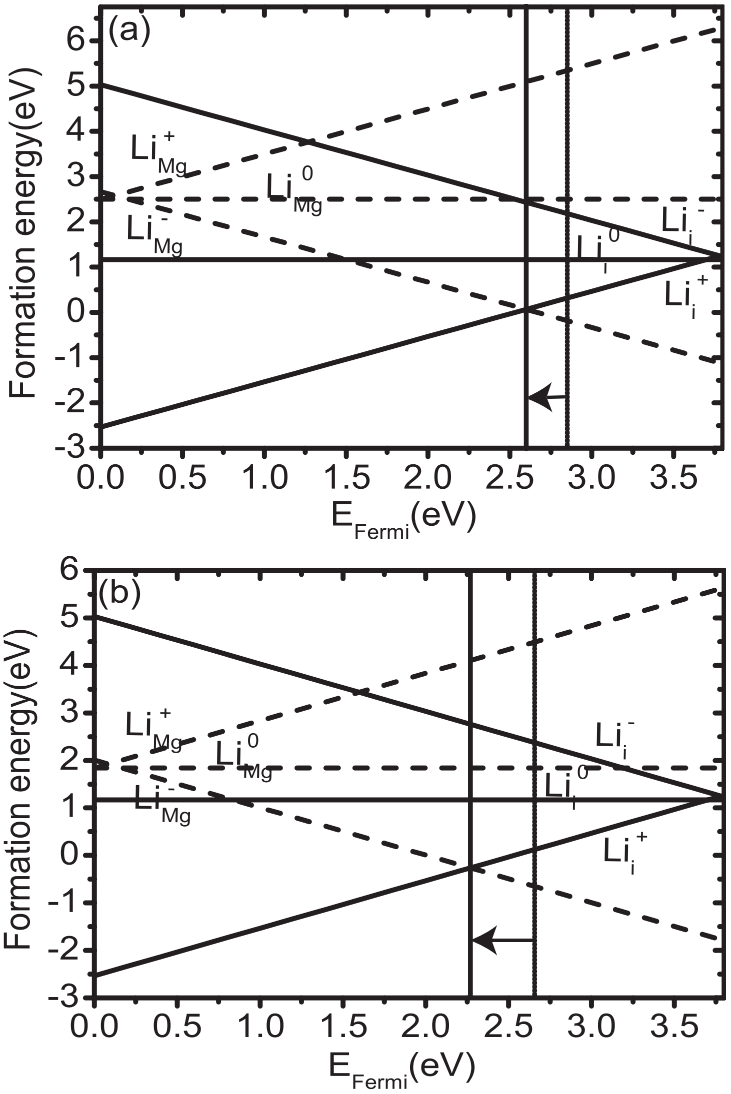

Figure 2.1. Formation energy of Li-dopant in MgH_2: (a) H-poor condition. (b) H-rich condition. The vertical solid and dashed lines indicate the Fermi energy in MgH_2 with and without Li, respectively. E_{Fermi}=0 eV corresponds to the VBM and E_{Fermi} = 3.8 eV corresponds to the CBM.

increased, leading to a higher activation barrier. Consequently, the Li doping makes the V_H^{+1} the dominant diffusion species in the whole range of H chemical potential.

We note that we have neglected entropy contribution in our analysis. Usually, this is a good approximation because the contribution due to the entropy difference is much smaller than the contribution due to the total energy difference. Of course, more accurate results can be obtained by calculating the phonon spectra of all the MgH_2 systems and H_2. On the other hand, for the MgH_2 system we consider, it has been shown that even though H has a low mass, the vibrational entropies for H in the lattice and in the H_2 reservoir are rather similar and hence the net entropy difference is small [14]. Also we have used a relatively large supercell dimension so that the added defect charge density in the supercell is very low. Consequently, the interaction energy between the charged defects in the neighboring cells is expected to be sufficiently small, and not to affect our conclusion.

The results above suggest the dominating defect and dopant species to be V_H^+, Li_{Mg}^{-1} and Li_i^{+1}. However, we did not consider the interaction between V_H^+ and Li_{Mg}^{-1}. Next, we calculated the attractive interaction energy between V_H^+ and Li_{Mg}^{-1} as a function of their separation, as shown in Fig. 2.2. We did not consider the interaction between V_H^+ and Li_i^{+1} because it is repulsive. Two key features are found in Fig. 2.2(b): (1) V_H^+ prefers to sit in one of the six nearest-neighbor H-sites (site 1 and site 2 in Fig. 2.2(a)) of Li with binding energy of 0.50-0.55 eV; (2) Once beyond the nearest-neighbor H-site, their attraction decays rapidly to be insignificant. Based on this observation, we propose a nearest-neighbor interaction model to determine how many V_H^+ are trapped by Li_{Mg}^{-1} as a function of Li doping concentration. We assume that the interaction energy is $\Delta\mathrm{E}_b$ = -0.55 eV when V_H^+ is in any of the six nearest-neighbor sites and negligible otherwise. Following the Boltzmann distribution [27], we have

$$R_{trapped} = \frac{3n\exp[-\Delta E_b/k_BT]}{[2N-3n]+3n\exp[-\Delta E_b/k_BT]} \tag{2.3}$$

where $\mathrm{R}_{trapped}$ is the ratio of the number of trapped V_H^+ to the total number of V_H^+, n is the number of doped Li, and N is the number of Mg sites. The number of substitutional and interstitial Li are taken to be the same under the charge-neutrality condition, as shown in Fig. 2.1.

Fig. 2.2(c) shows the calculated $\mathrm{R}_{trapped}$ as a function of Li doping concentration. We see that even in the low concentration (for example, $\frac{n}{N} = 1\times10^{-4}$), the trapping ratio $\mathrm{R}_{trapped}$ is very close to one, indicating that almost all the V_H^+ next to Li are immobilized due to their attractive interaction. This also indicates that H vacancy prefers to stay next to Li_{Mg}^{-1}, because its formation energy is effectively decreased by 0.55 eV.

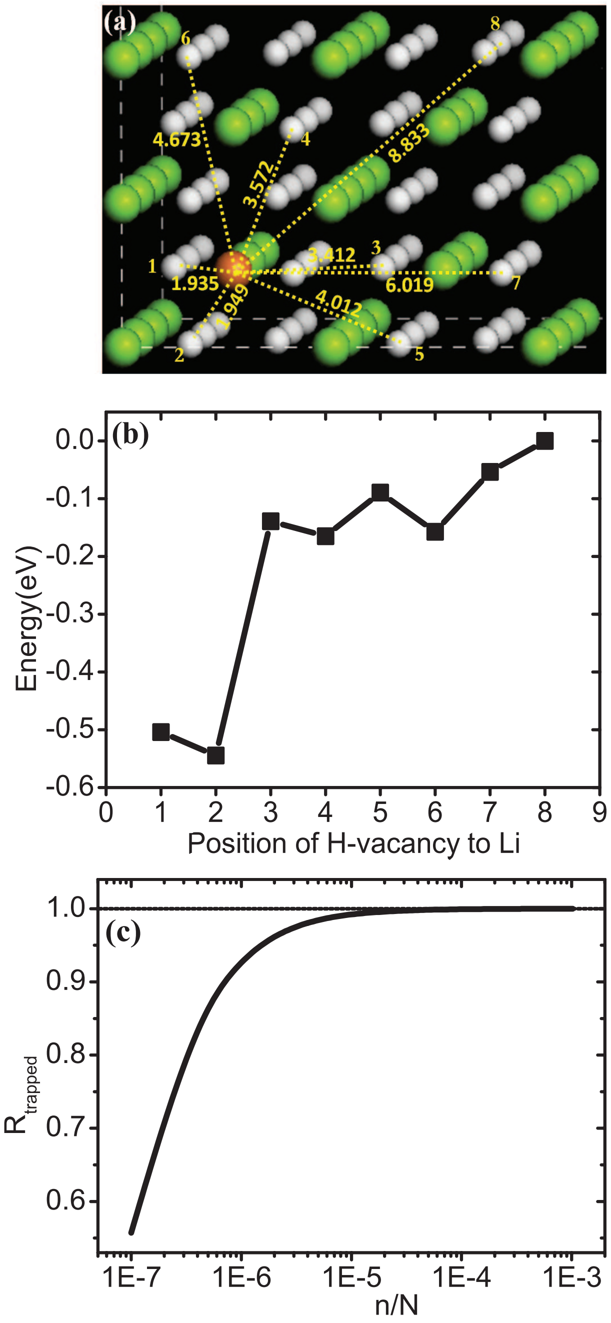

Figure 2.2. Binding between V_H^+ and Li_{Mg}^{-1}: (a) The structure of Li-dopant plus H-vacancy with H-vacancy at different positions labeled with number and distance from Li. (b) Interaction energy between V_H^+ and Li_{Mg}^{-1} as a function of their separation distance (in Angstrom). (c) Ratio of the trapped V_H^+ with Li_{Mg}^{-1} to the number of V_H^+, T = 400 K. Green balls are Mg atoms, white balls are H atoms, and orange ball is Li dopant.

Furthermore, we studied kinetically how H-vacancy diffusion is affected by the presence of Li_{Mg} through the calculation of diffusion barriers. In Fig. 2.3, we show the barriers for the H-vacancy diffusing from the nearest-neighbor sites of Li (sites 1 and 2 in Fig. 2.3(a)) to its closest H site (sites 4 and 5) (path 1) and from the next nearest-neighbor site (site 3) to its closet H site (site 5) (path 2). For the path 1, the diffusion barrier is found to increase by 0.15 eV compared to that in the undoped $\mathrm{MgH_2}$. For the path 2, the diffusion barrier is found only ∼30 meV higher than that in the undoped $\mathrm{MgH_2}$. This strong site dependence of H-vacancy diffusion barrier is consistent with the fast decay of the attractive interaction between V_H and Li_{Mg}, as shown in Fig. 2.2(b). The 0.15 eV increase of diffusion barrier, together with the large V_H trapping ratio, suggest that H vacancies will mostly be immobilized in the vicinity of Li dopants, inhibiting the V_H-mediated H diffusion.

2.4 Conclusion

In conclusion, we have investigated the effects of Li-doping in $\mathrm{MgH_2}$ on the H-vacancy-mediated H-diffusion, using DFT calculations. The formation energy calculation shows that the Li dopant favors two charged configurations of Li_{Mg}^{-1} and Li_{i}^{+1}. The charge neutrality condition requires the Fermi energy be shifted towards the VBM by 0.25 eV and 0.39 eV upon Li doping under the H-poor and H-rich conditions, respectively, which decreases the formation energy of V_H^{+} by the same amount. This leads to an increase of V_H^{+} concentration by up to about 5 orders of magnitude at T=400 K. Furthermore, the calculations of interaction energy between V_H^{+1} and Li_{Mg}^{-1} as well as diffusion barrier of H vacancy in the presence of Li show that almost all the H-vacancy next to Li are immobilized. Therefore, the H-diffusion is enhanced by Li doping in $\mathrm{MgH_2}$ only at the low Li doping concentration but not at the high concentration.

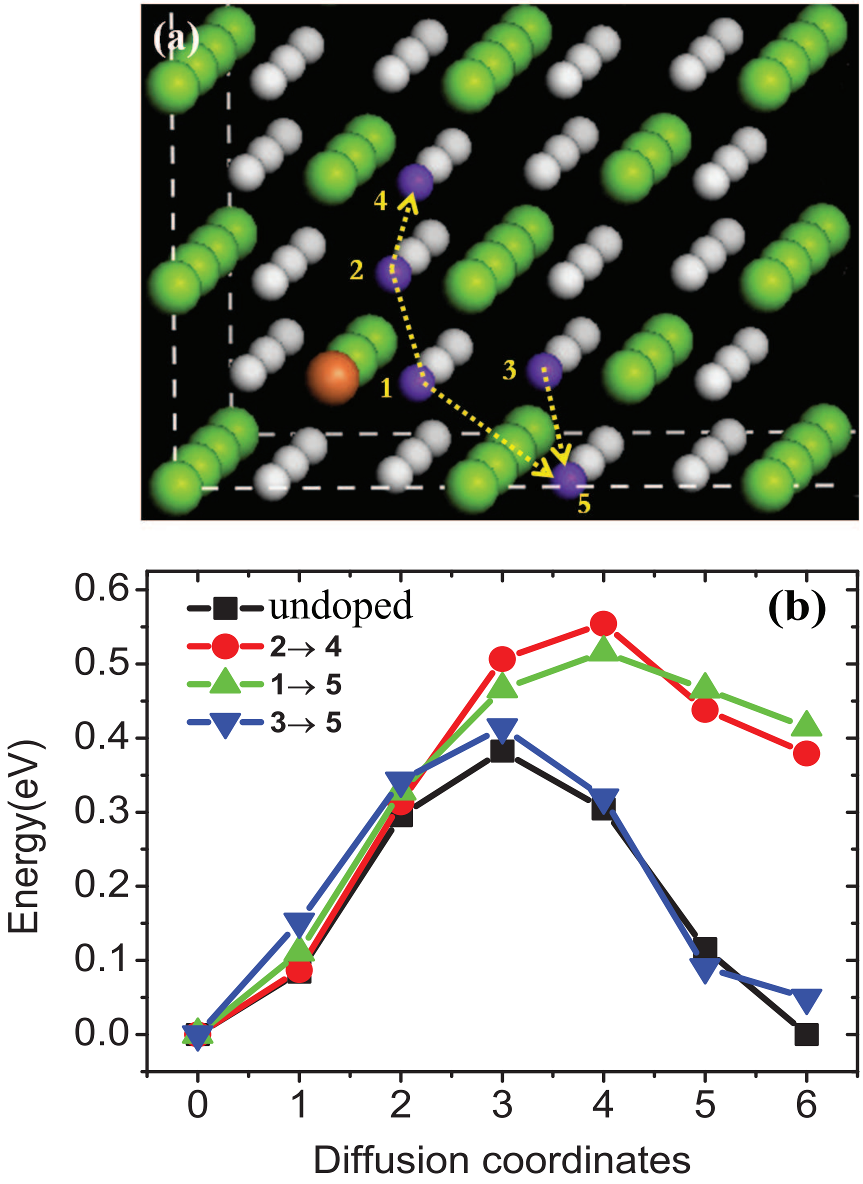

Figure 2.3. Effect of Li presence on V_H diffusion: (a) Illustration of different diffusion path for V_H to diffuse further away from Li site. The arrow indicates diffusion direction; (b) V_H-mediated H-diffusion barrier change with the presence of Li. The purple ball indicates the position of V_H in our calculation. The arrow indicates the diffusion path.

2.5 References

[1] P. Selvam, B. Viswanathan, C. S. Swamy and V. Srinivasan, Int. J. Hydrogen Energy **11**, 169 (1986).

[2] W. Klose and V.Stuke, Int. J. Hydrogen Energy **20**, 309 (1995).

[3] F. H. Ellinger, et al., J. Am. Chem. Soc. **77**, 2647 (1955).

[4] K. Zeng, T. Klassen, W. Oelerich and R. Bormann, Int. J. Hydrogen Energy **24**, 989 (1999).

[5] T. Noritake, M. Aoki, S. Towata, Y. Seno and Y. Hirose, Appl. Phys. Lett. **81**, 2008 (2002).

[6] B. Bogdanovi, K. Bohmhammel, B. Christ, A. Reiser, K. Schlichte R. Vehlen and U. Wolf, J. Alloys Compd. **282**, 84(1999).

[7] B. Sakintuna, F. Darkrim and M. Hirscher, Int. J. Hydrogen Energy **32**, 1121 (2007).

[8] M. Pozzo and A. Alfe, Phys. Rev. B **77**, 104103(2008).

[9] R. Yu and P. Lam, Phys. Rev. B **37**, 8730(1988)

[10] H. Reule, M. Hirscher, A. Weiβhardt and H. Kronmuller, J. Alloys Compd. **305**, 246(2000).

[11] N. Hanada, T. Ichigawa and H. Fujii, J. Phys. Chem. B **109**, 7188(2005).

[12] P. Larsson, C. Araujo, J. Larsson, P. Jena, and R. Ahuja, Proc. Natl. Acad. Sci. U. S. A. **105**, 8227(2008).

[13] A. Baldi, M. Silveira, V. Palmisano, B. Dam and R. Griessen, Phys. Rev. Lett. **102**, 226102(2009).

[14] A. Peles and C. Van de Walle, Phys. Rev. B. **76**, 214101(2007).

[15] S. Hao and D. Sholl, Appl. Phys. Lett. **93**, 251901(2008).

[16] N. Umezawa, M. Sato and K. Shiraishi, Appl. Phys. Lett. **93**, 223104(2008).

[17] S. Hao and D. Sholl, Appl. Phys. Lett. **94**, 171909(2009).

[18] Mi Park, A. Janotti and C. Van de Walle, Phys. Rev. B **80**, 064102(2009).

[19] K. Hoang and C. Van de Walle, Phys. Rev. B **80**, 214109 (2009).

[20] K. Smith, T. Fisher, U. Waghmare and R. Crespo, Phys. Rev. B **82**, 134109(2010).

[21] G. Kresse and D. Joubert, Phys. Rev. B **59**, 1758 (1999).

[22] J. P. Perdew, J. A. Chevary, S. H. Vosko, K. A. Jackson, M. R. Pederson, D. J. Singh and C. Fiolhairs, Phys. Rev. B **46**, 6671 (1992).

[23] G. Kresse and J. Furthmuller, Phys. Rev. B **54**, 11169 (1996).

[24] G. Mills and H. Jonsson, Phys. Rev. Lett. **72**, 1124 (1994).

[25] C. Van de Walle and J. Neugebauer, J. Appl. Phys. **95**, 3851(2004).

[26] S. Na-phattalung, M. J. Smith, K. Kim, M. H Du, S. H. Wei, S. B. Zhang and S. Limpijumnong, Phys. Rev. B **73**, 125205 (2006).

[27] G. H. Lu, Q. Wang and Feng Liu, App. Phys. Lett. **92**, 211906 (2008).

CHAPTER 3

TUNING NUCLEATION DENSITY OF METAL ISLAND WITH CHARGE DOPING OF SUBSTRATE

3.1 Introduction

Because of the ideal two-dimensional honeycomb crystal structure and exotic linearly dispersed electronic band structure, graphene has attracted intensive research effort in surface functionalization by external adsorbates in order to incorporate carrier doping [1, 2], magnetism [3, 4], catalysis [5, 6], superconductivity [7], and surface plasmon [8, 9], which are strongly related to the interfacial bonding involving orbital hybridization and charge transfer between adsorbate and graphene. Due to its only one-atom thickness, epitaxial graphene is usually unintentionally doped with a finite concentration of charge carriers through substrate charge transfer [10]. A wider range of charge doping can also be realized via electric field effect [11] or substrate doping [12]. Besides affecting the intrinsic graphene properties [13, 14], the resulting charge effect, on one hand, may alter the bonding strength between adsorbate and graphene, affecting adsorption and diffusion [15]; on the other hand, it may modulate the adsorbate-adsorbate interaction [16], affecting adsorbate island nucleation. Similar electronic tailing of adsorbate-substrate and adsorbate-adsorbate interactions were observed experimentally on ultrathin oxide film supported on a metallic substrate by varying the thickness of the oxide film [17].

For weakly corrugated metallic surfaces such as M/M(111) (M=Al, Cu, Ag, Au)) [18-21], the perturbation to the adsorbate diffusion barrier due to the existence of surrounding adsorbates beyond the nearest-neighbor (NN) distance is comparable to the adsorbate diffusion barrier. The resulting interadsorbate repulsion at intermediate distance leads to effective increase of the diffusion barrier, giving rise to significantly larger nucleation island density observed than what is estimated from mean-field nucleation theory that includes only NN interaction. Recent experiments of Fe deposited on epitaxial graphene on 6H-SiC(0001) [22] reported that island number density increases almost linearly with depositon coverage up to 2.5 ML without saturation and shows weak temperature dependence. These are the indications of graphene being another weakly corrugated system for Fe with sizeable interadatom repulsion at distances larger than the NN distance. Further spin density functional theory (sDFT) calculation reveals the electronic origin of the Fe-Fe repulsion [23].

In this work, we are motivated to study the charge doping effects on the Fe adsorption, diffusion, and adatom-adatom interaction on a graphene substrate. We found that hole doping increases the adsorption energy, diffusion barrier, and Fe-Fe repulsion energy, while electron doping decreases the diffusion barrier and only modifies slightly the adsorption energy and Fe-Fe repulsion energy. It is therefore expected that higher Fe island density can be achieved by hole doping and that more layer-like film can be achieved by electron doping. Further kMC simulations shows that Fe nucleation island number density can be tuned from being six times larger under hole doping to being ten times smaller under electron doping than the case without doping. This wide-range tunability may provide the potential to grow Fe film with either an island morphology as the magnetic storage device or a uniform layer morphology as the magnetic electric contact for spin injection in spintronic applications. It may also be used as a way to control metal morphology on graphene for plasmonic applications [24].

3.2 Calculation details

The sDFT calculations were performed by using projector augment wave pseudopotential [25] with the generalized gradient approximation [26] to the exchange-correlation functional, as implemented in the VASP package [27]. A 7×7 graphene supercell plus 13 Å vacuum was used as the substrate. 400 eV energy cutoff and $3 \times 3 \times 1$ Γ-centered k-mesh were used for wavefunction expansion and k-space integration, respectively. Charge doping was simulated by adding (removing) electrons for electron (hole) doping and compensating opposite charge background to keep the system neutral. The charge was varied from hole concentration of $-1.17 \times 10^{14}/cm^2$ to electron concentration of $0.78 \times 10^{14}/cm^2$. One Fe adatom was used to calculate the adsorption energy, diffusion barrier, and magnetic property. Two Fe atoms with varying separation were used to calculate the interatomic interaction energy. All the structures were relaxed in terms of internal atomic coordinates using conjugate gradient method until the force exerted on each atom is smaller than 0.01 eV/$\AA$. The transition saddle point along the adatom diffusion path was identified using the nudged elastic band method [28].

3.3 Results and discussion

First we found that within the doping concentration considered here, Fe adsorption site is the hollow site (H-site) and the transition saddle point is the bridge site (B-site). The adsorption energy E_{ad} is defined as $E_{ad} = E(Graphene + Fe) - E(Graphene) - E(Fe)$, where $E(Graphene + Fe)$ is the energy of adatom+graphene, $E(Graphene)$ is the energy of graphene with charge doping, and $E(Fe)$ is the energy of the isolated Fe atom. It is plotted as a function of charge doping concentration for Fe at both H-site and B-site in Fig. 3.1(a). With respect to the case without doping, hole doping increases rapidly the adsorption energy but electron doping only slightly changes the adsorption energy. Fe adsorption breaks the graphene π bond to form a Fe-C bond formation, so the adsorption energy is proportional to the bond energy difference between the Fe-C and the π bonds. Thus, the charge doping dependence of Fe-C bond energy and graphene π bond energy will determine the trend of Fe-adsorption energy as a function of charge doping concentration. Either hole or electron doping lowers the graphene π bond energy, because the former removes electrons from bonding states and the latter adds electrons in the antibonding states. For Fe-C bond formation, it involves charge transfer and orbital hybridization. The energy gain due to the charge transfer is proportional to the difference between electron energy levels of Fe atom before adsorption and the Fermi energy of graphene. Electron (hole) doping increases (decreases) Fermi energy, so the difference between electron energy levels of an isolated Fe atom and substrate Fermi energy will become larger for hole doping, indicating more charge transfer from Fe to graphene, but smaller for electron doping, indicating less charge transfer. Therefore, the combined effect of graphene π bond breaking and charge transfer may increase Fe adatom adsorption energy with hole doping but only slightly varies with electron doping.

We further calculated the change of Fe adatom charge transfer in response to graphene work function change (equivalently Fermi energy change) under charge doping in Fig. 3.1(b). The amount of charge transfer from the Fe adatom to graphene is represented by the Bader charge. As argued above, there is more charge transfer under hole doping and less charge transfer under electron doping for Fe at both the H-site and B-site. We may separate the adsorption energy into two parts including the contributions from the chemical bonding and electron charge-transfer with the following model:

$$E_{ad}(q) = E_r(q) - q\phi \tag{3.1}$$

where q is the amount of adatom charge transfer, ϕ is the graphene substrate work function and E_r is the remaining contribution from chemical bonding to the adsorption energy. The

E_{ad} variation due to change of bonding, work function, and charge transfer can be estimated with respect to that of intrinsic graphene+Fe using:

$$\Delta E_{ad}(q) = \Delta E_r(q) - q\Delta\phi - \phi\Delta q \tag{3.2}$$

While it is not clear in what fashion the first term $\Delta E_r(q)$ changes E_{ad}, we can easily determine that the second term increases E_{ad} in hole doping and decreases E_{ad} in electron doping when the work function is increased and decreased, respectively. Similarly, the third term increases E_{ad} in hole doping and decreases E_{ad} in electron doping when the charge transfer q is increased and decreased, respectively. Therefore, the second and third terms together predict an increase of E_{ad} under hole doping and an decrease of E_{ad} under electron doping. It is consistent with the analysis from the point of view of bond energy difference.

The Fe-adatom diffusion barrier is shown in Fig. 3.1(c) as a function of charge doping concentration. Without charge doping, the diffusion barrier is 0.48 eV, in good agreement with a previous report [29]. With hole doping, the diffusion barrier can be increased to 0.55 eV, but with electron doping, the diffusion barrier can be decreased to 0.28 eV. This trend can again be understood from the charge doping effect on the adsorption energy of Fe at the H-site and B-site, because the diffusion barrier is the adsorption energy difference at these two sites, which can be expressed as:

$$E_d(q) = E_r^B(q) - E_r^H(q) - (q_B - q_H)\phi \tag{3.3}$$

The first order variation of E_d in charge doping will then become:

$$\begin{aligned} \Delta E_d(q) = \quad & \Delta(E_r^B(q) - E_r^H(q)) - (q_B - q_H)\Delta\phi \\ & -\Delta(q_B - q_H)\phi \end{aligned} \tag{3.4}$$

The second term indicates that a direct tuning of work function ϕ will lead to a variation of diffusion barrier depending on the sign of work function change and the magnitude. Because work function is increased with hole doping, this term gives rise to an increase of diffusion barrier. On the other hand, because work function is decreased with electron doping, this term gives rise to a decrease of diffusion barrier. This predication is consistent with the trend of the diffusion barrier in Fig. 3.1(c) calculated from DFT. We thus believe the work function tuning should play the dominant role in varying the Fe-adatom diffusion barrier.

Without charge doping, previous work [30, 31] has shown that because of the hybridization between Fe $3d$ states and graphene p states, the Fe $4s$ states are shifted to higher energy relative to Fe $3d$ states upon adsorption and two originally occupying $4s$ electrons

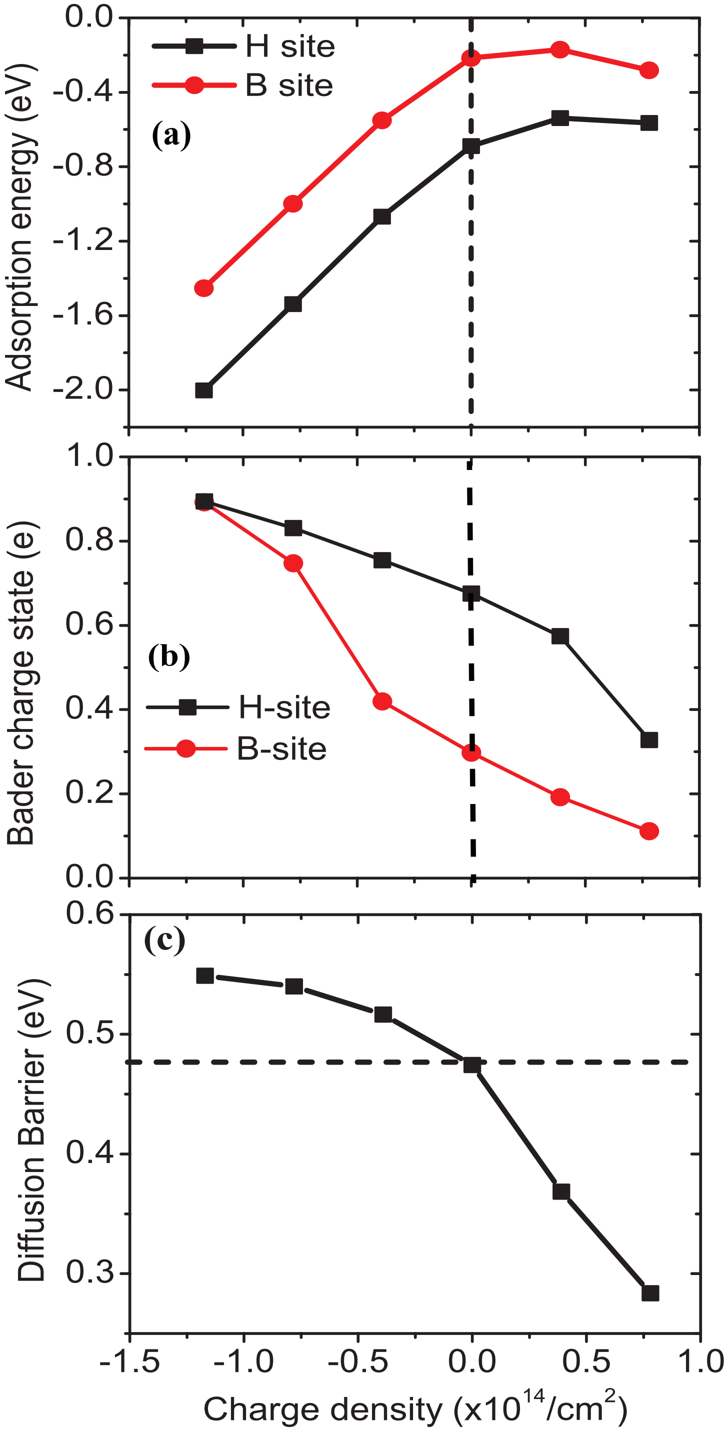

Figure 3.1. Charge doping effects on Fe adatom properties on graphene substrate: (a) Adsorption energy versus charge doping concentration for Fe adatom at H-site and B-site. (b) Bader charge of Fe adatom at H-site and B-site versus charge doping concentration. (c) diffusion barrier versus charge doping concentration.

are transferred mainly to Fe $3d$ states, resulting in a Fe local magnetic moment reduction from 4 μ_B to about 2 μ_B. Such a situation is expected to be further modified upon charge doping, which may change the Fe adatom orbital occupation. In Fig. 3.2(a), we show the Fe adatom local magnetic moment versus the charge doping concentration. Hole doping significantly increases the magnetic moment from 2.05 μ_B to 2.73 μ_B, and electron doping modestly increases the magnetic moment to 2.32 μ_B. In Fig. 3.2(b), the partial spin density of states for Fe s, p, and d orbitals under different charge doping concentrations are plotted. We can see that the Fe adatom orbital occupation changes with charge doping, which leads to the Fe magnetic moment variation with charge doping. With increasing hole doping, the occupation of the spin-down component of the Fe d-orbital keeps decreasing and the occupation of the spin-up component is almost unchanged. This results in an increase of Fe magnetic moment. With increasing electron doping, the slight decrease in Fe spin-down d-orbital occupation and increase in Fe spin-up s-orbital result in a slow increase of Fe magnetic moment.

Next we calculated Fe adatom-adatom interaction energy as a function of the adatom-adatom separation under different charge doping. Six configurations are considered, as shown in Fig. 3.3(a), in increasing order of separation. For clarity, we separated the NN adatom-adatom interaction (configuration 1), which represents the direct chemical bonding, from the beyond NN adatom-adatom interaction. They are shown in Fig. 3.3(b) and Fig. 3.3(c), respectively. The NN interaction energy is only changed very little under doping concentrations from $0.78 \times 10^{14}/cm^2$ to $-0.39 \times 10^{14}/cm^2$. However, one observes that larger hole doping decreases the NN interaction energy rapidly to be only 0.60 eV under the doping concentration of $-1.17 \times 10^{14}/cm^2$ with respect to 1.45 eV for the no-doping case. Recalling in Fig. 3.1(b) that the Bader charge keeps increasing from electron doping to hole doping, we may attribute this reduction of NN interaction energy to the significantly increased repulsive Coulomb interaction under large hole doping, which counteracts the attractive chemical bonding. In contrast, the adatom-adatom interaction under the doping concentration from $0.78 \times 10^{14}/cm^2$ to $-0.39 \times 10^{14}/cm^2$ may only take on much weaker dipole-dipole repulsive interaction than the direct Coulomb repulsive interaction under large hole doping, so that the net interaction energy is still close to that without doping. In Fig. 3.3(c), the adatom-adatom distance at which they display repulsive interaction persistently exists. Apparently, the repulsive peak is pushed gradually towards the next NN distance and the magnitude is increased from electron doping to hole doping, suggesting that the Coulomb interaction becomes increasingly significant with increasing hole doping.

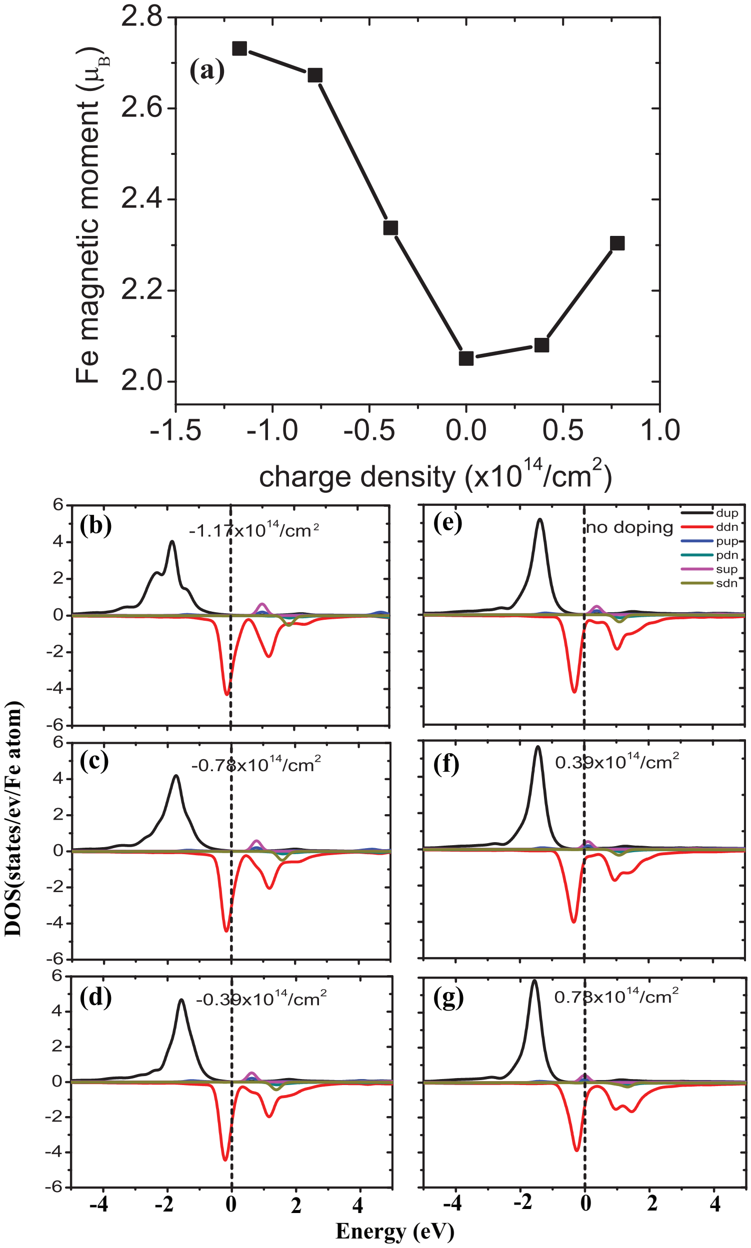

Figure 3.2. Charge doping effect on Fe adatom magnetic properties: (a) Local magnetic moment of Fe adatom of H-site versus charge doping concentration. (b-g) Fe adatom partial density of states with projection to s, p, d orbitals for both spin-up (sup, pup, and dup) and spin-down (sdn, pdn, and ddn) components.

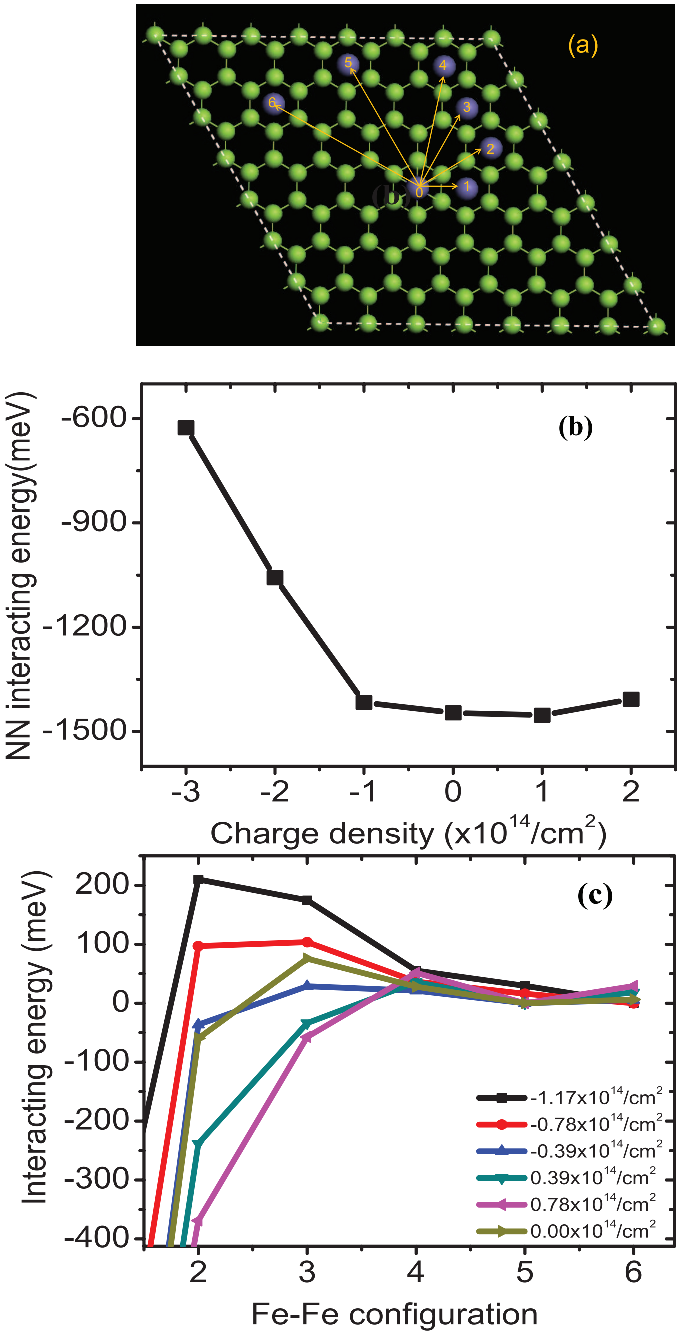

Figure 3.3. Charge doping effect on Fe interadatom interaction: (a) The six Fe-Fe configurations in increasing order of separation. The configuration is labeled with 1-6 accordingly, relative to the center Fe adatom. (b) Interaction energy between two NN Fe adatoms. (c) Interaction energy as a function of separation beyond NN.

The charge doping effects on the Fe-adatom diffusion barrier and adatom-adatom interaction are expected to be reflected in the Fe nucleation island number density at the initial stage of film growth. We next simulated the Fe island density as a function of charge doping concentration using kMC simulation method [32]. The simulation cell size used is a 200×200 graphene supercell. The diffusion barrier and adatom-adatom interactions from DFT calculations above were used as input parameters. The hopping rate with Arrhenius form of $\nu = \nu_0 \exp(-E_d/k_B T)$ and position-dependent diffusion barrier approximation of $E_d = E_d^0 + 0.5(E_j - E_i)$ were used. ν_0 is chosen to have constant value of $10^{12}/s$, T is 300 K, and E_i and E_j are the interaction energies before and after hopping, respectively. For simplicity, irreversible nucleation (no desorption), critical island size of 1, and no edge diffusion are assumed [33, 34]. The deposition rate is 0.01 ML/s and the amount of deposition is 0.05 ML. In Fig. 3.4, we show the island density for situations with and without including Fe adatom-adatom interaction. From the curve without adatom-adatom interaction, the island density can be decreased by 8 times under electron doping and increased by 3 times larger under hole doping. Including Fe adatom-adatom interaction, it is most evident that at hole doping larger than $-0.39 \times 10^{14}/cm^2$, the island density is significantly increased by up to 6 times. For the remaining doping regime, the island density is very close to that without interadatom interaction. It indicates that the combined effect of the diffusion barrier and interadatom interaction on the island density only takes place in large hole doping and the diffusion barrier tuning dominates the change of island density in the other charge doping regime.

3.4 Conclusion

To conclude, we have investigated the effect of the charge doping of graphene substrate on Fe nucleation island density, which increases under hole doping and decreases under electron doping. The underlying mechanism is the charge-tuning of the Fe-adatom diffusion barrier, which is gradually increased by hole doping but is rapidly decreased by electron doping, and Fe interadatom repulsive interaction, which is increased significantly by large hole doping. Additionally Fe local magnetic moment can be tuned significantly with charge doping. The combined effects provide a large range of tuning of island density and the growth morphology of metal nanostructure for spintronics and plasmonics applications via surface charge doping.

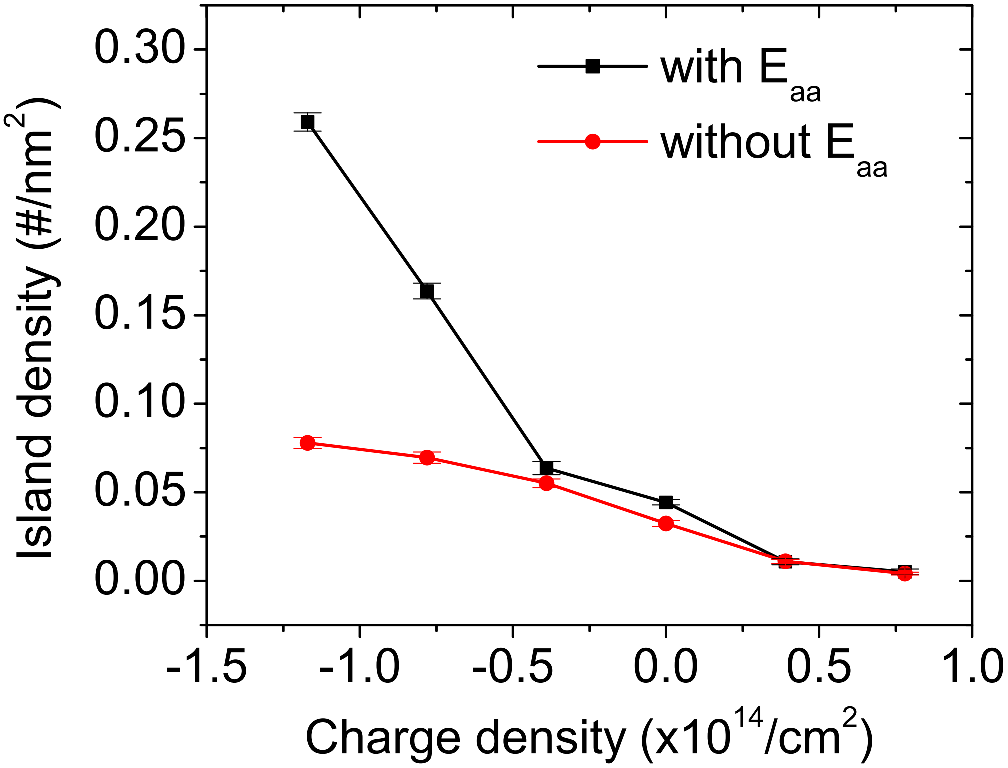

Figure 3.4. kMC simulated island number density as a function of charge doping concentration for both cases: with adatom-adatom interaction (with E_{ad}) and without adatom-adatom interaction (without E_{ad}).

3.5 References

[1] Aaron Bostwick, Taisuke Ohta, Thomas Seyller, Karsten Horn and Eli Rotenberg, Nat. Phys. **3**, 36 (2007).

[2] S. Y. Zhou, D. A. Siegel, A. V. Fedorov and A. Lanzara, Phys. Rev. Lett. **101**, 086402 (2008).

[3] T. Eelbo, M. Wasniowska, P. Thakur, M. Gyamfi, B. Sachs, T. O. Wehling, S. Forti, U. Starke, C. Tieg, A. I. Lichtenstein and R. Wiesendanger, Phys. Rev. Lett. **110**, 136804 (2013).

[4] A. V. Krasheninnikov, P. O. Lehtinen, A. S. Foster, P. Pyykkö, and R. M. Nieminen, Phys. Rev. Lett. **102**, 126807 (2009).

[5] Dr. Shaojun Guo, Sen Zhang, Liheng Wu and Prof. Shouheng Sun, Angew. Chem. Int. Ed. **51**, 11770 (2012).

[6] Kun Han, Peng Miao, Hui Tong, Tao Liu, Wenbo Cheng, Xiaoli Zhu and Yuguo Tang, Appl. Phys. Lett. **104**, 053101 (2014).

[7] Gianni Profeta, Matteo Calandra and Francesco Mauri, Nat. Phys. **8**, 131 (2012).

[8] Fred Schedin, Elefterios Lidorikis, Antonio Lombardo, Vasyl G. Kravets, Andre K. Geim, Alexander N. Grigorenko, Kostya S. Novoselov and Andrea C. Ferrari, ACS Nano 4, 5617 (2010).

[9] Jierong Cheng, Wei Li Wang, Hossein Mosallaei and Efthimios Kaxiras, Nano Lett. 14, 50 (2014).

[10] C. Riedl, C. Coletti, T. Iwasaki, A. A. Zakharov and U. Starke, Phys. Rev. Lett. **103**, 246804 (2009).

[11] Kin Fai Mak, Felipe H. da Jornada, Keliang He, Jack Deslippe, Nicholas Petrone, James Hone, Jie Shan, Steven G. Louie and Tony F. Heinz, Phys. Rev. Lett. **112**, 207401 (2014).

[12] Nisha Mammen, Shobhana Narasimhan and Stefano de Gironcoli, J. Am. Chem. Soc. **133**, 2801 (2011).

[13] C. Si, W. Duan, Z. Liu, and F. Liu, Phys. Rev. Lett. **109**, 226802 (2012).

[14] C. Si, W. Duan, Z. Liu, and F. Liu, Phys. Rev. Lett. **111**, 196802 (2013).

[15] J. O. Sofo, A. M. Suarez, Gonzalo Usaj, P. S. Cornaglia, A. D. Hernndez-Nieves and C. A. Balseiro, Phys. Rev. B **83**, 081411(R) (2011).

[16] Dmitry Solenov, Chad Junkermeier, Thomas L. Reinecke and Kirill A. Velizhanin, Phys. Rev. Lett. **111**, , 115502 (2013).

[17] Livia Giordano, Gianfranco Pacchioni, Jacek Goniakowski, Niklas Nilius, Emile D. L. Rienks and Hans-Joachim Freund, Phys. Rev. Lett. **101**, 026102 (2008).

[18] Kristen A. Fichthorn and Matthias Scheffler, Phys. Rev. Lett. **84**, 5371 (2000).

[19] Jascha Repp, Francesca Moresco, Gerhard Meyer, Karl-Heinz Rieder, Per Hyldgaard and Mats Persson, Phys. Rev. Lett. **85**, 2981 (2000).

[20] A. Bogicevic, S. Ovesson, P. Hyldgaard, B. I. Lundqvist, H. Brune and D. R. Jennison, Phys. Rev. Lett. **85**, 1910 (2000).

[21] Fabien Silly, Marina Pivetta, Markus Ternes, Franois Patthey, Jonathan P. Pelz and Wolf-Dieter Schneider, Phys. Rev. Lett. **92**, 016101 (2004).

[22] S. M. Binz, M. Hupalo, Xiaojie Liu, C. Z. Wang, Wen-Cai Lu, P. A. Thiel, K. M. Ho, E. H. Conrad and M. C. Tringides, Phys. Rev. Lett. **109**, 026103 (2012).

[23] Xiaojie Liu, C. Z. Wang, M. Hupalo, Wen-Cai Lu, P. A. Thiel, K. M. Ho and M. C. Tringides, Phys. Rev. B **84**, 235446 (2011).

[24] F. Moresco, M. Rocca, T. Hildebrandt and M. Henzler, Phys. Rev. Lett. **83**, 2238 (1999).

[25] G. Kresse and D. Joubert, Phys. Rev. B **59**, 1758 (1999).

[26] J. P. Perdew, J. A. Chevary, S. H. Vosko, K. A. Jackson, M. R. Pederson, D. J. Singh and C. Fiolhairs, Phys. Rev. B **46**, 6671 (1992).

[27] G. Kresse and J. Furthmuller, Phys. Rev. B **54**, 11169 (1996).

[28] Wenmei Ming, Zhigang Zak Fang and Feng Liu, J. App. Phys **114**, 243502 (2013).

[29] Oleg V. Yazyev and Alfredo Pasquarello, Phys. Rev. B **82**, 045407 (2010).

[30] Chao Cao, Min Wu, Jianzhong Jiang and Hai-Ping Cheng, Phys. Rev. B **81**, 205424 (2010).

[31] Kevin T. Chan, J. B. Neaton and Marvin L. Cohen, Phys. Rev. B **77**, 235430 (2008).

[32] K. A. Fichthorn and W. H. Weinberg, J. Chem. Phys. 95, 1090 (1991).

[33] M. C. Bartelt and J. W. Evans, Phys. Rev. B **46**, 12675 (1992).

[34] F. Liu, A. H. Li, and M.G. Lagally, Phys. Rev. Lett. **87**, 126103 (2001).

CHAPTER 4

STRAIN ENGINEERING OF IDEAL RASHBA STATES ON LAYERED SEMICONDUCTOR SURFACE

4.1 Introduction

The Rashba effect refers [1] to spin splitting of 2D electronic states as a result of a perpendicular electric field in the presence of SOC. Much recent effort has been made in studying this effect in solid state systems for potential spintronics applications, such as spin field transistor [2] and the intrinsic spin Hall effect [3]. The degree of spin splitting, quantified by the Rashba parameter α, scales with the strength of the electric field and SOC. The earliest realization of the Rashba effect was made in the asymmetric quantum well formed in InGaAs/InAlAs heterostructure [4], with small spin splitting. Nobel metal (e.g., Au [5], Ag [6] and Ir [7]) and *sp*-orbit heavy-metal surfaces (e.g., Bi [8], Sb [9] and Pb [10]) were shown to have large spin splitting. Heavy metal adatoms alloying with metal (e.g., Bi/Ag(111) [11]) and/or semiconductor surfaces (e.g., Si(111) [12]) were found to possess giant Rashba splitting. Most recently, new surface systems with Rashba splitting have been reported in graphene [13] and topological insulators [14-16]. However, because the substrates previously adopted are either metal or a semiconductor with strong dangling bonds, typically Rashba surface states are overwhelmed by the large number of spin-degenerated substrate states, hindering their practical applicability.

There are two apparent conditions to realize large Rashba spin splitting: a large SOC and a large electric field. It has been recently demonstrated by both theory [17] and experiment [18] that these two conditions can be met by surface electronic states formed at the Te-terminated surface of bismuth tellurohalides, BiTeX (X = I, Br and Cl), a peculiar family of polar semiconductors. The Bi atoms provide the required large SOC, while the underlying polar semiconductor substrate provides a large electric field at the surface. Most significantly, the resulting Rashba states are situated completely inside the bulk band gap. Consequently, they are called ideal Rashba states, because they are separated in energy from the spin-degenerated bulk states, so that the surface transport of Rashba states is isolated from the bulk carrier contribution. In this chapter, based on first-principles electronic structure and nonequilibrium Green's function transport calculations, we demonstrate an alternative approach to realize ideal Rashba effect by strain engineered growth of a Au single layer on the layered large band-gap semiconductor β-InSe(0001) substrate. It exploits a physical mechanism different from BiTeX, with the Au overlayer providing the strong SOC while the Au/InSe(0001) interface gives rise to the polarization.

4.2 Results and discussion

The bulk phase of β-InSe has a large band gap of 1.2 eV [19]. It has a layered crystal structure, with each layer consisting of Se-In-In-Se atomic planes and stacking along z direction. Within each layer, In and Se are bonded covalently; between layers, they are bonded with van der Waals (vdW) interaction. Its in-plane lattice constant is $4.05\AA$. The atomic structure of Au/InSe(0001) is shown in Fig. 4.1(a-b) for side and top views, respectively. The first-principles calculation are carried out based on density function theory with projector augment wave pseudopotential [20] and Perdew-Burke-Ernzerhof [21] exchange-correlation functional using the VASP package [22]. All the atoms are allowed to relax until the forces are smaller than 0.01 eV/Å. Six hundred eV kinetic energy cutoff and 11×11×1 Γ centered k-mesh sampling are adopted for total energy convergence. The substrate is simulated by 7 layers of (1×1)-InSe(0001) with a vacuum layer of more than 20Å.

The interlayer binding energy between Au and InSe(0001) is $\sim$ 0.5 eV/surface-unit-cell. This indicates that the surface interaction is in an "intermediate" range [23], slightly stronger than the vdW bond but significantly weaker than the typical chemical bond. Fig. 4.2(a) shows the corresponding band structures of Au/InSe(0001) along $M - \Gamma - K$ directions. The shaded area represents the substrate states and the two separate lines are the surface states, (whose location will be seen more clearly in the later discussion of charge distribution). Importantly, the two surface bands show a large Rashba spin splitting at k-points from midpoint of $M - \Gamma$ to midpoint of $\Gamma - K$ and is mostly inside in the substrate band gap. Therefore, naturally by itself, this system can already significantly reduce the effect of substrate carriers, having two advantages: (1) the substrate has a large band gap; (2) on one hand, its surface interaction with Au is weak enough to avoid strong hybridization between the surface and substrate states; on the other hand, it is strong enough to induce a large Rashba spin splitting. However, in the vicinity of Γ, the Rashba surface bands are

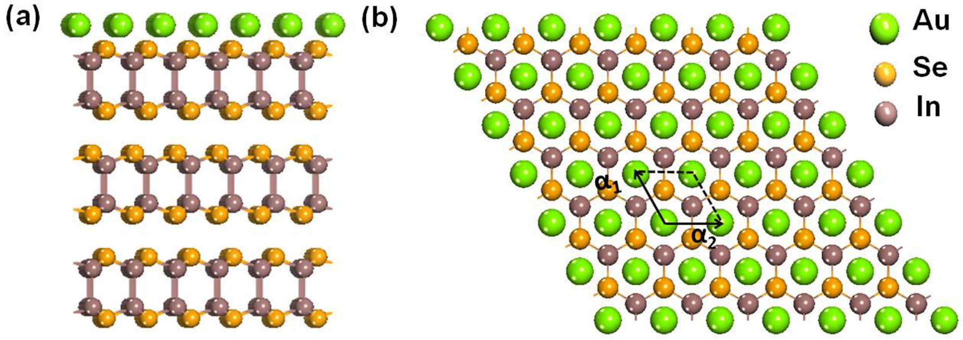

Figure 4.1. Atomic structure of Au/InSe(0001): (a) Side view of the (6×6) supercell structure of Au grown on layered InSe(0001) substrate, which is shown with only the top three layers for clarity. (b) Top view of the supercell. α_1 and α_2 represent the surface unit cell vectors.

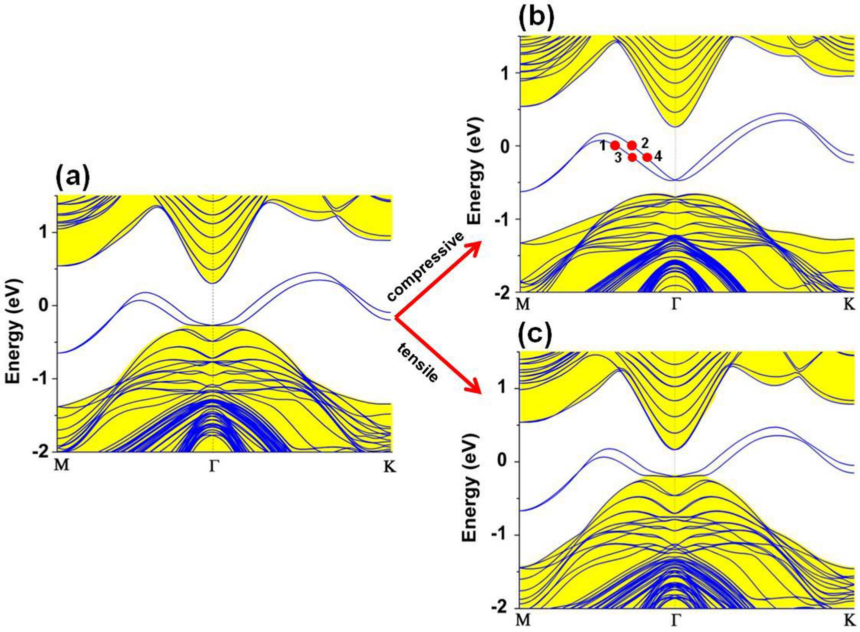

Figure 4.2. Band structures of Au/InSe(0001) under different strain cases: (a) strain-free. (b) Compressive strain = -1.2%. (c) Tensile strain = +1.2%.

buried by the substrate states.

Next, we demonstrate by strain engineering the formation of "ideal" Rashba states from the Rashba surface bands above. We applied both compressive and tensile biaxial strains to the substrate to tune the relative position of the surface and the underlying substrate bands. Compressive strain is found to reduce the overlap between the surface and substrate bands, and the surface bands becomes situated completely inside the band gap of the substrate under a compressive strain of -1.2%, as shown in Fig. 4.2(b). This can be attributed to the substrate band gap enlargement due to the down-shifting and up-shifting of the valence and conduction bands, respectively, relative to the surface bands. In contrast, tensile strain exerts an opposite effect that the overlap between the surface and substrate bands increases, and the band gap shrinks, with the up-shifting and down-shifting of the valence and conduction bands, respectively, as seen under a tensile strain of $+1.2\%$ in Fig. 4.2(c). This tunable band positioning under strain indicates different deformation potentials for valence, conduction and the surface bands [24], respectively. In the following, all the results shown are for the ideal Rashba states engineered by a -1.2% strain, corresponding to a strained lattice constant of ~ 4 $\mathring{A}$.

We have identified the asymmetric potential responsible for the Rashba spin splitting and the nonzero $\alpha \propto \int \partial V(z)/\partial z dz$ [25]. The in-plane averaged potential $V(z) = \frac{1}{A}\int V(x,y,z)dxdy$, where A is the surface area, along z direction is shown in Fig. 4.3(a). The red dashed box indicates the region of Au and the first layer of the substrate, where electrons experience an asymmetric potential. In the remaining region, however, the potential is symmetric and almost identical for each layer to that in the bulk. This indicates that the Rashba states are localized only in the top Au+InSe layer. We further confirm this by calculating the local charge distribution for the Rashba states 1-4 as labeled in Fig. 4.2(b) at each atomic plane from the top-most Au plane to the bottom-most Se plane, as shown in Fig. 4.3(b-e). The red dashed boxes show that the charge of each state is mostly distributed in the first five atomic planes, beyond which it is negligibly small. An implication from this spatial localization of the Rashba states is that even a small thickness of substrate such as only one layer of InSe(0001) can be used to realize similar ideal Rashba states, which is a useful feature for producing strain in InSe(0001) grown on another substrate. Moreover, from a tight-binding point of view, Rashba spin splitting originates from the atomic Stark effect [26] under the potential-asymmetry-induced electric field and SOC; therefore the Rashba wavefunction must contain orbital compositions such as s/p_z and p_z/d_{z^2}, which have opposite parities in the z direction to have nonzero Stark matrix elements. This is

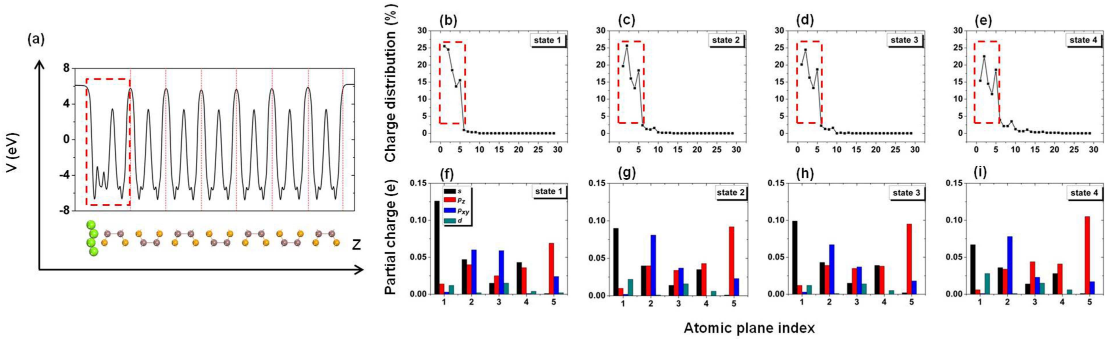

Figure 4.3. Rashba states spatial localization: (a) Plane-averaged potential V along z-axis. (b-e) Charge distribution of the Rashba states 1-4, as labeled in Fig. 4.2(b) as as a function of the atomic plane. (f-i) Orbital compositions in the first five atomic planes for the Rashba states 1-4.

indeed confirmed by plotting orbital compositions of the Rashba states 1-4 in Fig. 4.3(f-i), which all contain large amounts of s, p_z and small amounts of d_z^2 components at each atomic plane.

Furthermore, we show the spin polarization texture of the Rashba states in Fig. 4.4. The spin polarization is defined: $\overrightarrow{p}(\overrightarrow{k}) = [< S_x(\overrightarrow{k}) >, < S_y(\overrightarrow{k}) >, < S_z(\overrightarrow{k}) >]$, where $< S_\alpha(\overrightarrow{k}) > = < \psi(\overrightarrow{k})|\sigma_\alpha|\psi(\overrightarrow{k}) >, (\alpha = x, y, z)$. It is plotted at two iso-energy surfaces of E = 0.0 eV and -0.12 eV. Blue and red colors represent outer and inner branches of the Rashba bands, respectively. Overall, the iso-surface is isotropic for the inner circle with smaller k-vector, but gains some anisotropy of hexagonal shape for the outer circle with larger k-vector. The z-component of the spin polarization is about ten times smaller than the x- and y- components, and the in-plane spin polarization is nearly perpendicular to the k-vector. This spin polarization texture is very similar to that in the 2D Rashba SOC free-electron gas, which has only in-plane spin distribution [27]. Because the spin polarization texture reflects the k-dependent effective Rashba SOC magnetic field, the spin polarization of a spin-up electron injected into a free-electron gas channel with Rashba SOC was shown to oscillate sinusoidally over its travel length by spin-precession [28]. Hence, Au+InSe(0001) is expected to possess a similar sinusoidal spin oscillation effect. Thus, we fit the Rashba bands to the standard free-electron Rashba band dispersion. The fitted Rashba parameter is 0.45 eV$\mathring{A}$. It corresponds to a characteristic spin precession length [29] L_{so} ($=$ $(\frac{\pi}{\alpha})(\frac{\hbar^2}{2m})$), where m is the electron effective mass, of ~50 $\mathring{A}$, over which electron up-spin is rotated to down-spin, and the periodicity of the sinusoidal oscillation is $2L_{so} =$ ~100 $\mathring{A}$.

The spin-dependent electron conductance is calculated to reveal the electron spin oscillation effect in Au/InSe(0001). From the wavefunctions of the Rashba bands of first-principle calculation, the maximally localized Wannier functions are constructed by using the Wannier90 package [30]. The two Wannier functions obtained do not resemble any simple atomic orbitals, but hybridized orbitals with comparable distribution at both the top Au layer and the first layer of the InSe substrate. An effective tight-binding Hamiltonian of the Rashba bands is then obtained using the two Wannier functions as a basis. A two-terminal nanoribbon device is constructed with the width of $4a$ (a is the surface lattice constant of InSe(0001)), as shown in Fig. 4.5(a). The left lead is ferromagnetic and the right lead is nonmagnetic. We assume no SOC in the lead regions by artificially setting the Hamiltonian matrix elements of the spin-flip term to zero, and the channel region has the SOC as described by the full effective Hamilton. Fig. 4.5(b) shows the band structure of

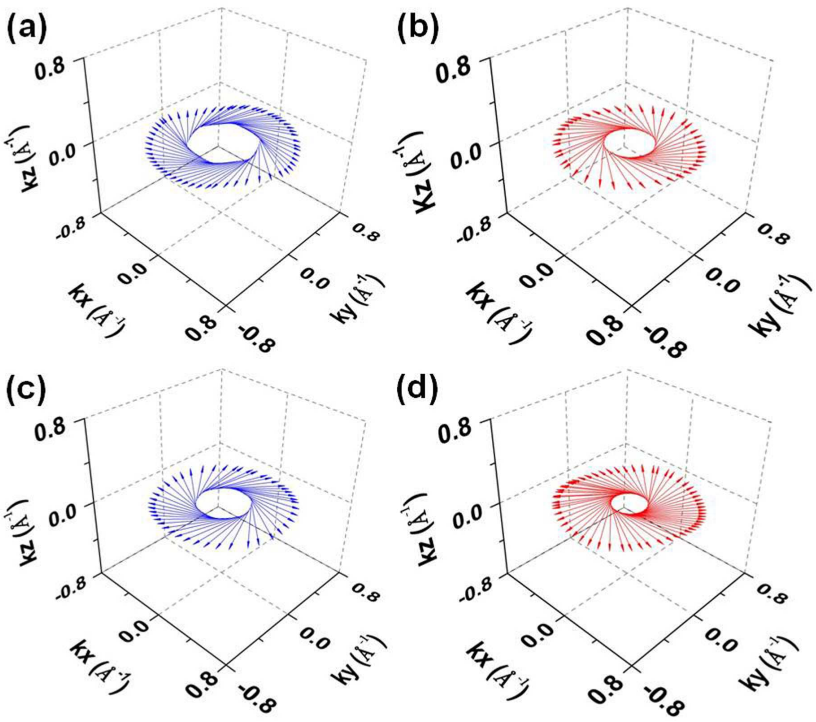

Figure 4.4. Spin polarization textures of the Rashba bands at two iso-energy surfaces of E = 0.0 eV (a-b) and E = -0.12 eV (c-d), respectively.

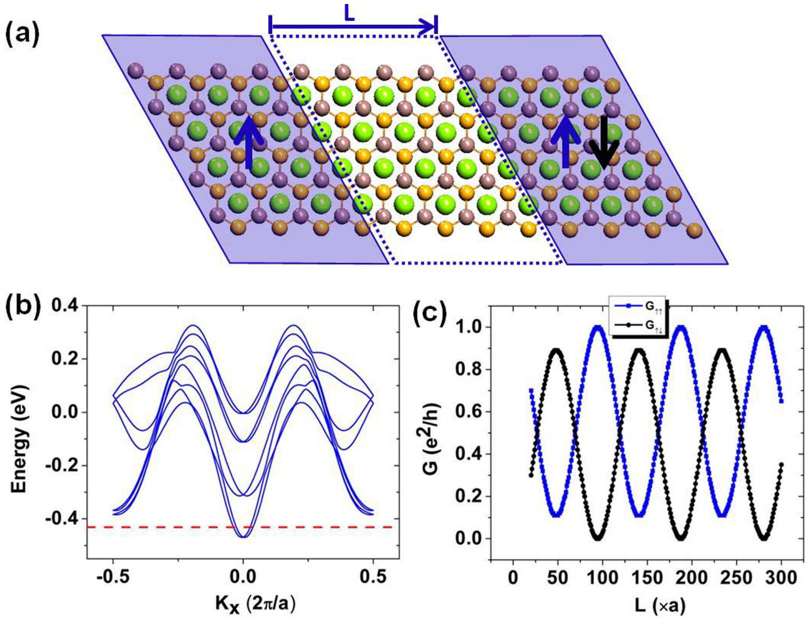

Figure 4.5. Spin transistor designed from Au/InSe(0001) nanoribbon: (a) Two-terminal devive setup: the boxes on the left and on the right represent source and drain leads without SOC, respectively. The left lead is ferromagnetic and the right lead is nonmagnetic. The middle dashed-line box represents the channel with Rashba SOC. (b) The band structure of the channel when assuming periodic structure in transport direction (L). The red dashed line shows the Fermi energy position used in the conductance calculation. (c) The spin-up $G_{\uparrow\uparrow}(E_F)$ and spin-down $G_{\uparrow\downarrow}(E_F)$ contributions to the total conductance, as a function of device length (L).

the channel region assuming a periodic boundary condition along the transport direction (L)). The Fermi energy is chosen to be at the position indicated by the red dashed line, crossing only two bands with Rashba splitting. The small width of the device gives rise to a transverse confinement potential, so that the spin-degenerate states, which are seen in Fig. 4.2 around Brillouin-zone corner (e.g., M and K), do not appear around the Fermi energy, leaving only the bands with Rashba SOC. On the other hand, our further calculation shows that significant increase of the ribbon width eventually brings down those spin-degenerate states to the same energy window of the Rashba bands, which should be avoided.

The conductance $G(E_F)$ of the device is calculated using nonequilibrium Green's function method and Landauer-B$\ddot{u}$ttiker formalism [31]:

$$G_{pq}(E_F) = \frac{e^2}{h} Tr(\Gamma_{lp} G^R \Gamma_{rq} G^A), \tag{4.1}$$

where $G^R = G^{A+}$ is retarded Green function of the channel, Γ describes the interface coupling between the lead and the channel, and p,q are spin indexes. In Fig. 4.5(c), $G_{\uparrow\uparrow}(E_F)$ and $G_{\uparrow\downarrow}(E_F)$ are plotted for the spin-up and spin-down contributions to the total conductance, respectively, as a function of channel length (L). They both exhibit nearly perfect sinusoidal oscillation with periodicity of $\sim 90a$ (~ 360 $\mathring{A}$). This oscillation periodicity from the nanoribbon configuration is ~ 4 times as large as that estimated from the 2D configuration. We confirm this increased oscillation periodicity by fitting the nanoribbon band structure to free-electron Rashba SOC band dispersion. We find that the Rashba parameter α is reduced to ~ 0.25 eV$\mathring{A}$ and the effective mass m is reduced to be about half of that for 2D configuration. Therefore the oscillation periodicity $2L_{so}$ is increased by ~ 4 times, which is consistent with the increase from conductance calculation. The change of α and m should be originated from the interplay between the comparable strengths of transverse potential confinement and Rashba SOC in the channel. This results in finite interband mixing and consequent modified Rashba band dispersion, similarly studied in Ref. [28, 32].

Lastly, we point out that the compressive strain, which is critical for realizing the ideal Rashba bands in Au/InSe(0001), can be achieved by epitaxially growing InSe(0001) thin film on a semiconductor substrate with smaller lattice constant. Several substrates can be chosen such as GaAs(111), AlAs(111), ZnSe(111) and Ge(111), which all have surface lattice constant ~ 4 $\mathring{A}$, and hence impose the desired amount of strain on InSe(0001) thin film. On the other hand, InSe(0001) can be replaced by other layered semiconductor substrates such as those from metal chalcogenides family [33], and they may also exhibit ideal Rashba states upon heavy metal deposition.

4.3 Conclusion

In conclusion, we have demonstrated the formation of ideal Rashba states by strain engineering of heavy-metal film on a layered large band-gap semiconductor substrate. The first-principle band structure calculation of Au single layer on strained InSe(0001) has shown that the Rashba bands with large spin-splitting are situated completely inside the substrate band gap. It originates from a physical mechanism different from BiTeX, where the Au overlayer provides the strong SOC while the interface gives rise to the polarization. The sinusoidal spin oscillation effect is confirmed by the conductance calculation with nonequilibrium Green's function method. Our approach may be generalized to other metal overlayers and layered semiconductor substrates, which is useful to reduce the unwanted effect of substrate spin degenerate carriers on spintronics devices

4.4 References

[1] E. I. Rashba, Sov. Phys. Solid State **2**, 1109 (1960); Y.A Bychkov and E. I. Rashba, JETP Lett. **39**, 78 (1984).

[2] S. Datta, and Das, Appl. Phys. Lett. **56**, 665 (1990).

[3] Jairo Sinova, Dimitrie Culcer, Q. Niu, N. A. Sinitsyn, T. Jungwirth, and A. H. MacDonald, Phys. Rev. Lett. **92**, 126603 (2004).

[4] JunSaku Nitta, Tatsushi Akazaki, and Hideaki Takayanagi, Phys. Rev. Lett. **78**, 1335 (1997).

[5] S. LaShell, B. A. McDougall, and E. Jensen, Phys. Rev. Lett. **77**, 3419 (1996).

[6] D. Popovic, F. Reinert, S. Hufner, V. G. Grigoryan, M. Springborg, H. Cercellier, Y. Fagot-Revurat, B. Kierren and D. Malterre, Phys. Rev. B **72**, 045419 (2005).

[7] A. Varykhalov, D. Marchenko, M. R. Scholz, E. D. L. Rienks, T. K. Kim, G. Bihlmayer, J. Sanchez-Barriga, and O. Rader, Phys. Rev. Lett. **108**, 066804 (2012).

[8] Yu. M. Koroteev, G. Bihlmayer, J. E. Gayone, E. V. Chulkov, S. Blugel, P. M. Echenique, and Ph. Hofmann, Phys. Rev. Lett. **93**, 046403 (2004).

[9] K. Sugawara, T. Sato, S. Souma, T. Takahashi, M. Arai, and T. Sasaki, Phys. Rev. Lett. **96**, 046411 (2006).

[10] J. Hugo Dil, Fabian Meier, Jorge Lobo-Checa, Luc Patthey, Gustav Bihlmayer, and Jurg Osterwalder, Phys. Rev. Lett. **101**, 266802 (2008).

[11] Christian R. Ast, Jurgen Henk, Arthur Ernst, Luca Moreschini, Mihaela C. Falub, Daniela Pacile, Patrick Bruno, Klaus Kern, and Macro Grioni, Phys. Rev. Lett. **98**,

186807 (2007).

[12] I. Gierz, T. Suzuki, E. Frantzeskakis, S. Pons, S. Ostanin, A. Ernst, J. Henk, M. Grioni, K. Kern, and C. R. Ast, Phys. Rev. Lett. **103**, 046803 (2009).

[13] Yu. S. Dedkov, M. Fonin, U. Rudiger and C. Laubschat , Phys. Rev. Lett. **100**, 107602 (2008).

[14] Jin-Jian Zhou, Wanxiang Feng, Ying Zhang, Shengyuan A. Yang and Yugui Yao, Sci. Rep. **4**, 3841 (2014).

[15] P. D. C. King, R. C. Hatch, M. Bianchi, R. Ovsyannikov, C. Lupulescu, G. Landolt, B. Slomski, J. H. Dil, D. Guan, J. L. Mi *et al.*, Phys. Rev. Lett. **107**, 096802 (2011).

[16] Z.-H. Zhu, G. Levy, B. Ludbrook, C. N. Veenstra, J. A. Rosen, R. Comin, D. Wong, P. Dosanjh, A. Ubaldini, P. Syers, N. P. Butch, J. Paglione, I. S. Elfimov and A. Damascelli, Phys. Rev. Lett. **107**, 186405 (2011).

[17] S. V. Eremeev, I. A. Nechaev, Yu. M. Koroteev, P. M. Echenique and E. V. Chulkov, Phys. Rev. Lett. **108**, 246802 (2012).

[18] M. Sakano, M. S. Bahramy, A. Katayama, T. Shimojima, H. Murakawa, Y. Kaneko, W. Malaeb, S. Shin, K. Ono, H. Kumigashira *et al.* Phys. Rev. Lett. **110**, 107204 (2013).

[19] P. Gomes da Costa, R. G. Dandrea, R. F. Wallis and M. Balkanski, Phys. Rev. B **48**, 14135 (1993).

[20] G. Kresse and D. Joubert, Phys. Rev. B **59**, 1758 (1999).

[21] J. P. Perdew, K. Burke, and M. Ernzerhof, Phys. Rev. Lett. **77**, 3865 (1996).

[22] G. Kresse and J. Furthm*ü*ler, Comput. Mat. Sci. **6**, 15(1996).

[23] Z. Liu, C.-X. Liu, Y.-S. Wu, W.-H. Duan, Feng Liu, and J. Wu, Phys. Rev. Lett. **107**, 136805 (2011).

[24] Miao Zhou, Zheng Liu, Zhengfei Wang, Zhaoqiang Bai, Yuanping Feng, Max G. Lagally and Feng Liu, Phy. Rev. Lett, **111**, 246801 (2013).

[25] Miki Nagano, Ayaka Kodama, T Shishidou and T Oguchi, J. Phys.: Condens. Matter **21**, 064239 (2009).

[26] Hongki Min, J. E. Hill, N. A. Sinitsyn, B. R. Sahu, Leonard Kleinman and A. H. MacDonald, Phy. Rev. B **74**, 165310 (2006); Sergej Konschuh, Martin Gmitra, and Jaroslav Fabian, *ibid* **82**, 245412 (2010); K. V. Shanavas, Z. S. Popovic and S. Satpathy, *ibid* **90** 165108 (2014).

[27] Oleg Krupin, PhD dissertation "Dichroism and Rashba effect at magnetic crystal surfaces of rare-earth metals", Freie Universität Berlin, 2004.

[28] Francisco Mireles and George Kirczenow, Phy. Rev. B, **64**, 024426 (2001).

[29] Ming-Hao Liu, Son-Hsien Chen and Ching-Ray Chang, Phys. Rev. B **78**, 195413 (2008).

[30] Ivo Souza, Nicola Marzari and David Vanderbilt, Phys. Rev. B, **65**, 035109 (2001).

[31] Z. F. Wang and Feng Liu, Appl. Phys. Lett. **99**, 042110 (2011).

[32] A. V. Moroz and C. H. W. Barnes, Phy. Rev. B, **60**, 14272 (1999).

[33] A. Aruchamy, *Photoelectrochemistry and Photovoltaics of Layered Semiconductors*, Kluwer Academic, Netherlands, 1992.

CHAPTER 5

FORMATION OF QUANTUM SPIN HALL STATE ON SI SURFACE AND ENERGY GAP SCALING WITH STRENGTH OF SPIN ORBIT COUPLING

5.1 Introduction

Recently, there has been a surge in the investigation of topological insulators (TIs) [1-3]. TIs are characterized by topologically protected metallic surface or edge states with helical spin polarization residing inside an insulating bulk gap. These states have negligible elastic scattering and Anderson localization [4, 5], which may provide ideal dissipationless spin current for future electronic devices with low power consumption. To realize their potential applications, it is desirable for the TIs to have an energy gap as large as possible [6], i.e., for room temperature applications. As for 2D TIs [i.e., quantum spin Hall (QSH) insulators], they also need to be grown or placed onto a substrate [7-10] or formed as an interface [11, 12], while maintaining a large gap. One desired approach is to directly fabricate large-gap TIs on semiconductor surfaces, which may avoid problems like transfer or interfacing a 2D layer over a foreign substrate. So far, however, this goal remains elusive.

The HgTe quantum well, as the first theoretically predicted [11] and experimentally confirmed [12] QSH insulator, has a small gap of 40 meV with topological edge states only detectable at very low temperature (<10 K) [12]. Recent studies pertaining to Bi/Sb(111) films [13-16], Sn films [17], metal-decorated graphene [18 20], silicene/germanene [21], and 2D organometallic frameworks [22-25] have largely enriched the family of 2D TIs, and some of them have a large gap [13, 17, 20]. However, a critical drawback with most previous theoretical studies of 2D TIs is their reliance on the electronic and topological properties of freestanding films, whose existence can be in doubt. Even if a freestanding film does exist, its properties are expected to be influenced by the underlying substrate in real applications [8-10].

Here, we demonstrate a unique approach of creating QSH state on a conventional semiconductor surface via depositing heavy elements with strong spin orbit coupling (SOC) onto a patterned Si(111) surface into a hexagonal lattice, which exhibits a TI state with a large energy gap of ∼0.5 eV. Here, the substrate plays a 'positive' role acting as an orbital filter to critically select the orbital composition around the Fermi level to realize a nontrivial large-gap topological state [26]. Specifically, the surface system can be matched onto an effective four-band model Hamiltonian which captures the underlying physics. Furthermore, we depict a unified picture of energy gap as a function of SOC to achieve a large-gap QSH state. Importantly, we found that it is not always true to have a large gap with a heavier atom of larger SOC, a noteworthy point for future design of TIs.

5.2 Results and discussion

We have performed density functional theory (DFT)-based first-principles calculations of band structure and band topology of 2D hexagonal lattices of various metal atoms, including Bi, Pb grown on a patterned H-saturated Si(111) surface. The detailed methodologies are presented in the Supplementary Information [27]. We will first discuss in detail the results of Bi and Pb, as representative examples, and leave the results of other metals for later discussion. Atomically flat H-Si(111) surface has been prepared for decades and is a widely-used substrate for epitaxial growth of ordered overlayers [28, 29]. The surface dangling bonds are passivated by H to avoid surface reconstruction. In order to form a hexagonal metal overlayer lattice, we propose a two-step fabrication process, as shown in Fig. 5.1. First, to create a desirable surface template pattern for metal growth, H atoms are selectively removed in hexagonal symmetry using scanning tunneling microscopy, as discussed in Refs. [30, 31]; Second, heavy metal atoms with large SOC can be deposited to grow or self-assemble into the exposed Si sites, as already demonstrated for other systems [32-34].

We found a very strong binding between the deposited metal atoms and the exposed Si atoms in the H-Si(111) surface, as evidenced by the calculated adsorption length [d, see Fig. 5.1(c)] of 2.68 Å and 2.75 Å for Bi and Pb, respectively. The high structural stability is also indicated by a large adsorption energy (E_{ad}), defined as $E_{ad} = E_{M+H-Si(111)} - (2E_M + E_{H-Si(111)}) + E_{H_2}$, where $\mathrm{E}_{M+H-Si(111)}$, E_M , $\mathrm{E}_{H-Si(111)}$, and E_{H_2} denote the energy of Bi/Pb+H-Si(111), single metal atom, pristine H-Si(111) surface, and H_2 gas molecule, respectively. The adsorption energy is found to be 3.88 eV and 3.92 eV for Bi and Pb, respectively, which are much larger than the binding energies of bulk Bi (2.18 eV) and

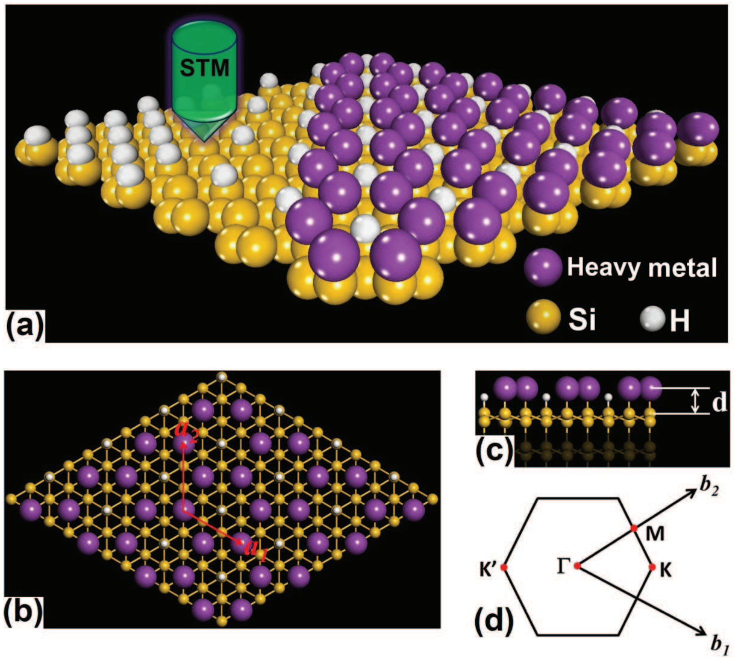

Figure 5.1. Experimental proposal to grow heavy atoms into hexagonal lattice: (a) Schematic of a two-step approach to fabricate 2D TI by deposition of heavy metal atoms on a patterned H-Si(111) surface. (b, c) The top and side view of the proposed structure, with the surface unit cell vector (a_1, a_2) indicated in (b) and the adsorption length d in (c). (d) The first surface Brillouin zone.

Pb (2.03 eV) in the crystalline solid form, indicating high thermodynamic stability of the surface systems.

To examine the band topology of such surface structures, we first purposely exclude SOC from calculation. The resulting band structures for Bi and Pb+H-Si(111) are shown in Figs. 5.2(a-b), respectively. For Bi+H-Si(111), there are two Dirac bands residing inside the bulk gap of Si with a Dirac point at K point, which locates nearby the Fermi level [Fig. 5.2(a)]. Analysis of band composition further showed that the two Dirac bands consist mainly of p_x orbitals of Bi atoms. Another dispersive band, consisting of p_y orbitals of Bi, sits below the bulk conduction band edge of Si and touches the upper Dirac band of p_x orbitals at Γ point. The band structure of Pb+H-Si(111) is similar to the case of Bi, represented by two Dirac bands inside the Si gap; but the Dirac point sits 0.8 eV above Fermi level and the upper Dirac bands largely overlap with the conduction band of Si [Fig. 5.2(b)]. Such different behaviors originate from the different valance electron configuration of Pb and Bi, e.g., $[Xe].4f^{14}.5d^{10}.6s^2.6p^2$ for Pb and $[Xe].4f^{14}.5d^{10}.6s^2.6p^3$ for Bi. With two electrons less in Pb+H-Si(111) per unit cell, the lower Dirac band becomes almost unoccupied compared to that of Bi+H-Si(111).

Next, we include SOC in calculation, and the resulting band structures of Bi and Pb+H-Si(111) are shown in Figs. 5.2(c) and (d), respectively. One sees that for Bi@H-Si(111), two Dirac bands are split apart; one large energy gap of ∼0.7 eV opens at K point, and another gap of 0.5 eV opens at Γ point, which is the global gap. The p_y and the upper p_x bands are also separated by SOC, with an indirect gap of 0.45 eV. We note that the spin degeneracy of these bands is lifted with most noticeable splitting at K point, which is due to the Rashba effect [35] induced by the broken spatial inversion symmetry. Although Rashba effect has been shown to be detrimental to QSH phase [18], in our systems such extrinsic spin splitting is relatively small compared to the intrinsic SOC-induced band gap [see Fig. 5.2(c)], suggesting the QSH state is robust against Rashba effect in our surface systems. It should also be noted that the SOC strength of Si is orders of magnitude smaller than Bi, making the SOC of Bi a decisive factor in opening the energy gap. Similarly, the SOC opens a gap at K point for Pb+H-Si(111), with the upper branch of Dirac bands moving completely into the Si conduction band, as shown in Fig. 5.2(d). Nevertheless, the energy splitting between the two Dirac bands is found to be around 0.65 eV at K point, and an effective SOC gap of 0.54 eV could be counted by the energy difference between the Si conduction band minimum and the top of the Pb p_x band. However, to truly make the Pb+H-Si(111) a 2D TI, n-type doping is needed to shift the Fermi level into the SOC gap,

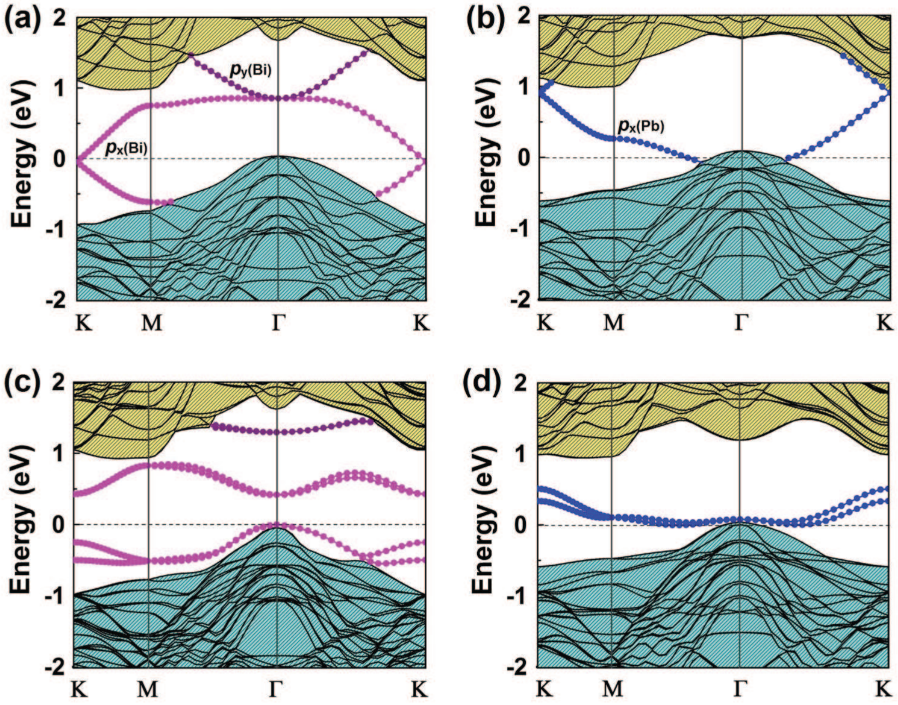

Figure 5.2. DFT Band structures of heavy metals on patterned Si(111): (a-b) Band structures of Bi and Pb+H-Si(111) without SOC, respectively. The Fermi level is set at zero. The green (yellow) shaded area represents the valence bands (conduction bands) of Si. Band compositions around Fermi level are also indicated. (c-d) Same as (a-c) with SOC.

such as by Si substrate doping or electric gating.

The SOC-induced gap opening at the Dirac point in Bi+H-Si(111) and Pb+H-Si(111) indicates possible existence of a 2D TI state. To check this, we calculated the topological edge states of Bi+H-Si(111) by the Wannier90 package [36]. Using DFT bands as input, we construct the maximally localized Wannier functions and fit a tight-binding Hamiltonian with these functions. Fig. 5.3(a) shows the DFT and fitted band structures, which are in very good agreement. Then, the edge Green's function of a semi-infinite Bi+H-Si(111) is constructed and the local density of state (DOS) of the Bi zigzag edge is calculated, as shown in Fig. 5.3(b). Clearly, one sees gapless edge states that connect the upper and lower band edge of the bulk gap, forming a 1D Dirac cone at the center of the Brillouin zone (Γ point). This indicates that the Bi+H-Si(111) is a 2D TI with a large gap of ~0.5 eV.

To further confirm the above topological edge-state results, we also calculated Z2 topology number. As the spatial inversion symmetry is broken in these systems, we used the method developed by Xiao et al. [21, 37]. In this method, Z_2 is calculated by considering the Berry gauge potential and Berry curvature associated with the Bloch wave functions, which does not require any specific point-group symmetry. Indeed, we found that $Z_2=1$ for Bi+H-Si(111), confirming the existence of QSH state in this surface. Assuming a shift of Fermi level above the lower branch of the Dirac band, we also found $Z_2=1$ for Pb+H-Si(111).

The physical origin of QSH state in Bi+H-Si(111) and Pb+H-Si(111) can be understood by a substrate orbital filtering effect as discussed recently in a related system of Bi on halogenated Si surfaces [26]. Fig. 5.3(c) shows the partial density of states (DOS) of Bi+H-Si(111) around the Fermi level. It is seen that the p_z orbital of Bi hybridizes strongly with the dangling bond of the exposed surface Si atom overlapping in the same energy range, which effectively removes the p_z bands away from the Fermi level, leaving only the p_x and p_y orbitals. We also analyzed the charge density redistribution [see upper panel of Fig. 5.3(d)], which clearly shows that charge redistribution induced by the Si surface mainly happens to the p_z orbital of Bi, in a similar way to the saturation of Bi p_z orbital by using hydrogen [lower panel of Fig. 5.3(d)]. It has been shown that the free-standing planar hexagonal lattice of Bi is a topologically trivial insulator with $Z_2=0$. When it is placed onto the H-Si(111) surface or adsorbed with H, it becomes topologically nontrivial. This originates from the intriguing orbital filtering effect imposed by the substrate or H saturation, which selectively removes the p_z orbitals from the Bi lattice to realize the large-gap QSH phase.

Specifically, we can describe the Bi+H-Si(111) using a simplified (p_x, p_y) four-band model Hamiltonian in a hexagonal lattice as [23,38],

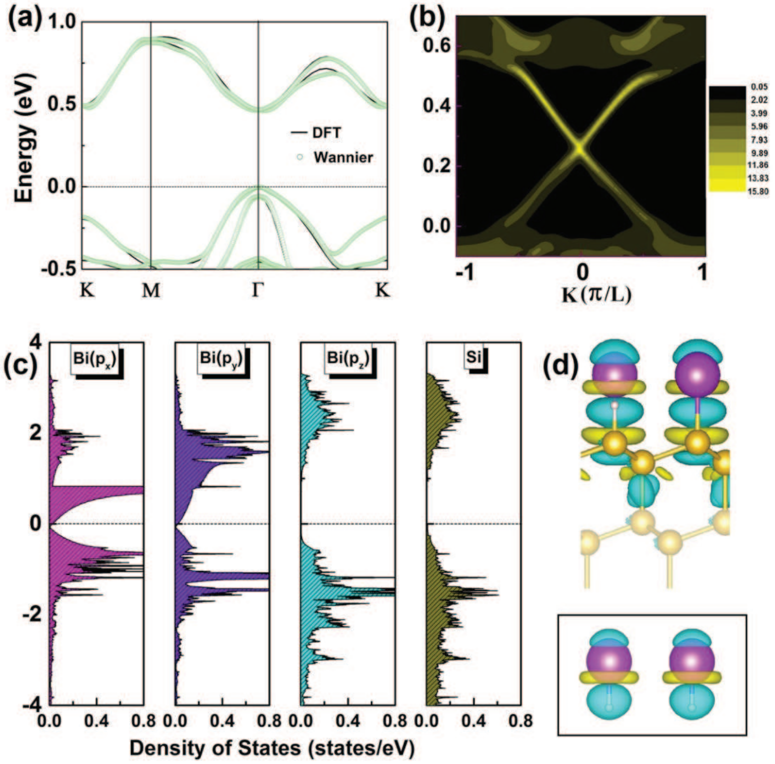

Figure 5.3. The edge states from the TI on Si(111): (a) Comparison of band structures for Bi+H-Si(111) calculated by DFT (black lines) and Wannier function method (green circles). (b) The Dirac edge states within the SOC-induced band gap. Scale bar is indicated on the right. (c) The partial DOS projected onto p_x, p_y , and p_z orbitals of Bi, and the total DOS of neighboring Si atoms. (d) Top: The charge density redistribution induced by metal atom surface adsorption for Bi+H-Si(111) (isovalue = 0.02 e/$\AA^3$), illustrating saturation of Bi p_z orbital. Bottom: Same as Top for the H-saturated freestanding planar Bi lattice.

$$\hat{H}_{eff} = \begin{pmatrix} \varepsilon_0 & 0 & S_{xx} & S_{xy} \\ 0 & \varepsilon_0 & V_{xy} & V_{yy} \\ S^*_{xx} & S^*_{xy} & \varepsilon_0 & 0 \\ S^*_{xy} & S^*_{yy} & 0 & \varepsilon_0 \end{pmatrix} + \sigma_z \lambda_{so} \begin{pmatrix} 0 & -i & 0 & 0 \\ i & 0 & 0 & 0 \\ 0 & 0 & 0 & -i \\ 0 & 0 & i & 0 \end{pmatrix}, \tag{5.1}$$

in which $S_{xx} = V_{pp\sigma} + (\frac{1}{4}V_{pp\sigma} + \frac{3}{4}V_{pp\pi}) \times (\exp(ika_1) + \exp(ik(a_1 + a_2)))$, $S_{xy} = \frac{3}{4} \times (V_{pp\sigma} + V_{pp\pi}) \times (\exp(ika_1) + \exp(ik(a_1 + a_2)))$, and $S_{yy} = V_{pp\pi} + (\frac{3}{4}V_{pp\sigma} + \frac{1}{4}V_{pp\pi}) \times (\exp(ika_1) + \exp(ik(a_1 + a_2)))$, a$_1$,a$_2$ is the lattice vector, $V_{pp\sigma}(V_{pp\pi})$ is the Slater-Koster parameter [39], and $\sigma_Z = \pm 1$ is the spin eigenvalue.

Diagonalization of Eq. (5.1) in reciprocal space gives the band structures shown in Fig. 5.4, which shows typical four bands as a function of SOC strength. One sees that without SOC, this Hamiltonian produces two flat bands and two Dirac bands with a Dirac point formed at K point and two quadratic points at Γ point [Fig. 5.4(a)]. Inclusion of a small SOC ($\lambda = 0.2$t) opens one energy gap (ΔE$_1$) at K point and two energy gaps (ΔE$_2$) at Γ point [Fig. 5.4(b)], with both gaps topologically nontrivial [23]. With the increasing SOC strength, both ΔE$_1$ and ΔE$_2$ increase [Fig. 5.4(c)], which eventually leads to the formation of a different energy gap (ΔE$_3$) between the upper and lower Dirac bands at Γ point when ΔE$_3$ becomes smaller than both ΔE$_1$ and ΔE$_2$ [Fig. 5.4(d)]. As such, for sufficiently large SOC, $\triangle$E$_3$ replaces $\triangle$E$_1$ to be the global gap, and correspondingly the global gap shifts from K to Γ point. Further increase of SOC will tend to decrease $\triangle$E$_3$, indicating that for sufficiently large SOC, the band gap decreases with increasing SOC.

Such an interesting phenomenon has also been confirmed by the DFT results. By comparing Bi+H-Si(111) and Pb+H-Si(111), we see that given the correct Fermi energy, the global gap is located at Γ point for Bi+H-Si(111) [Fig. 5.2(c)], but at K point for Pb+H-Si(111) [Fig. 5.2(d)]. This is because the SOC strength in p orbital of Pb (0.91 eV) is smaller than that of Bi (1.25 eV) [40]. Meanwhile, the energy gap between the two p$_x$ Dirac bands induced by SOC is actually larger for Pb+H-Si(111) (0.65 eV) than that of Bi+H-Si(111) (0.5 eV), suggesting that Pb may be a better choice to achieve large-gap QSH states on the substrate. This is in sharp contrast with the Kane-Mele model in graphene, for which an energy gap is opened at Dirac point that is in proportion to the strength of SOC [18].

5.3 Conclusion

In summary, we demonstrate the possibility of controlled growth of large-gap topological quantum phases on conventional substrate surfaces such as the important Si surface by a unique approach of substrate orbital filtering process combined with a proper choice of

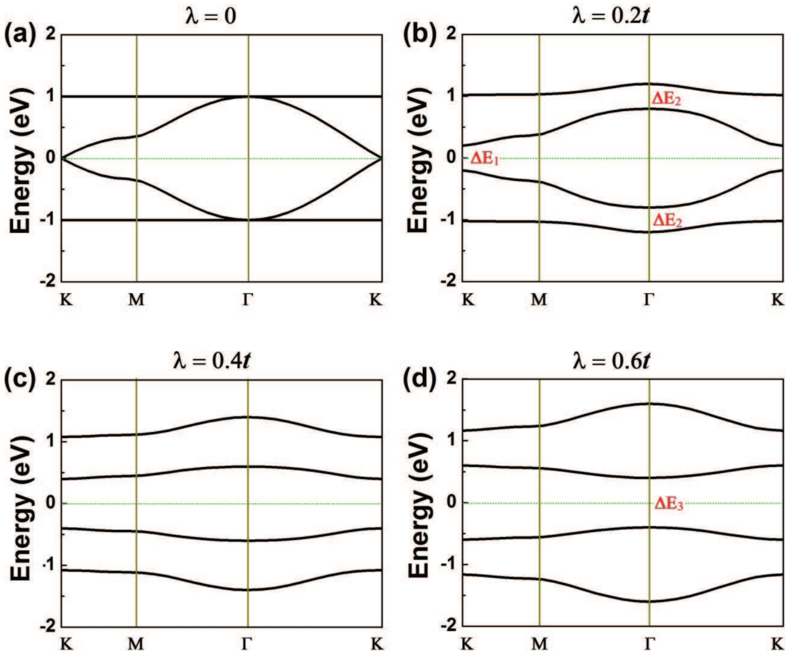

Figure 5.4. Energy bands resulting from the four-band model [Eq. (5.1)] as a function of SOC strength (λ) scaled by t (t is the coupling strength between neighboring p_x and p_y orbitals). Fermi energy is set to 0. The SOC-induced energy gaps (ΔE_1, ΔE_2, and ΔE_3) are indicated. The global gap transition from K point to Γ point driven by SOC can be clearly seen.

SOC. Its underlying physical principles are general, applicable to deposition of different metal atoms on different substrates. It opens up a new and exciting avenue for future design and fabrication of room temperature topological surface/interface states based on current available epitaxial growth and semiconductor technology.

5.4 References

[1] J. E. Moore, Nature **464**, 194 (2010).

[2] M. Z. Hasan, C. L. Kane, Rev. Mod. Phys. **82**, 3045 (2010).

[3] X.-L. Qi, S.-C. Zhang, Rev. Mod. Phys. **83**, 1057 (2011).

[4] B. A. Bernevig, S.-C. Zhang, Phys. Rev. Lett. **96**, 106802 (2006).

[5] C. Xu, J. E. Moore, Phys. Rev. B **73**, 045322 (2006).

[6] Y. Xia et al. , Nat. Phys. **5**, 398 (2009).

[7] F. Yang et al., Phys. Rev. Lett. **109**, 016801 (2012).

[8] T. Hirahara et al., Phys. Rev. Lett. **109**, 227401 (2012).

[9] L. Miao et al., Proc. Natl. Acad. Sci. U.S.A. **110**, 2758 (2013).

[10] Z. F. Wang et al., Nat. Commun. **4**, 1384 (2013).

[11] M. König et al., Science **318**, 766 (2007).

[12] Y. L. Chen et al., Science **325**, 178 (2009).

[13] S. Murakami, Phys. Rev. Lett. **97**, 236805 (2006).

[14] M. Wada, S. Murakami, F. Freimuth, G. Bihlmayer, Phys. Rev. B **83**, 121310 (2011).

[15] Z. Liu et al., Phys. Rev. Lett. **107**, 136805 (2011).

[16] P. F. Zhang, Z. Liu, W. Duan, F. Liu, J. Wu, Phys. Rev. B **85**, 201410 (2012).

[17] Y. Xu et al., Phys. Rev. Lett. **111**, 136804 (2013).

[18] C. L. Kane, E. J. Mele, Phys. Rev. Lett. **95**, 226801 (2005).

[19] C. Weeks, J. Hu, J. Alicea, M. Franz, Phys. Rev. X **1**, 021001 (2011).

[20] J. Hu, J. Alicea, M. Franz, Phys. Rev. Lett. **109**, 266801 (2012).

[21] C. C. Liu, W. Feng, Y. Yao, Phys. Rev. Lett. **107**, 076802 (2011).

[22] Z. F. Wang, Z. Liu, F. Liu, Nat. Commun. **4**, 1471 (2013).

[23] Z. Liu, Z. F. Wang, J. W. Mei, Y. S. Wu, F. Liu, Phys. Rev. Lett. **110**, 106804 (2013).

[24] Z. F. Wang, N. Su, F. Liu, Nano Lett. **13**, 2842 (2013).

[25] Z. F. Wang, Z. Liu, F. Liu, Phys. Rev. Lett. **110**, 196801 (2013).

[26] M. Zhou, W. Ming,Z. Liu, Z. F. Wang, P. Li, F. Liu, Proc. Natl. Acad. Sci. U.S.A. in press.

[27] Our electronic structure calculations based on density functional theory were performed by using a plane wave basis set and the projector-augmented wave method, as implemented in the VASP code. The exchange-correlation functional was treated with the generalized gradient approximation in Perdew-Burke-Ernzerhof format. Calculations of Z2 triviality were carried out by using the full-potential linearized augmented plane-wave method implemented in the WIEN2K package.

[28] G. S. Higashi, Y. J. Chabal, G. W. Trucks, K. Raghavachari, Appl. Phys. Lett. **56**, 656 (1990).

[29] H. Tada, T. Kawaguchi, A. Koma, Appl. Phys. Lett. **61**, 2021 (1992).

[30] T.-C. Shen et al., Science **268**, 1590 (1995).

[31] S. R. Schofield et al., Nat. Commun. **4**, 1649 (2013).

[32] K. K. Gomes, W. Mar, W. Ko, F. Guinea, H. C. Manoharan, Nature **483**, 306 (2012).

[33] M. Polini, F. Guinea, M. Lewenstein,, H. C. Manoharan, V. Pellegrini, Nat. Nanotechnol. **8**, 625 (2013).

[34] D. J. Michalak, et al., Nat. Mater. **9**, 266 (2010).

[35] Y. A. Bychkov, E. I. Rashba, JETP Lett. **39**, 78 (1984).

[36] A. A. Mostofi et al., Comput. Phys. Commun. **178**, 685 (2008).

[37] W. X. Feng, J. Wen, J.-J. Zhou, D. Xiao, Y. G. Yao, Comput. Phys. Commun. **183**, 1849 (2012).

[38] C. Wu, S. Das Sarma, Phys. Rev. B **77**, 235107 (2008).

[39] J. C. Slater,G. F. Koster, Phys. Rev. **94**, 1498 (1954).

[40] G. Bian, X. Wang, T. Miller, T.-C. Chiang, Phys. Rev B **88**, 085427 (2013).